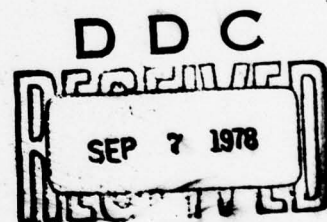
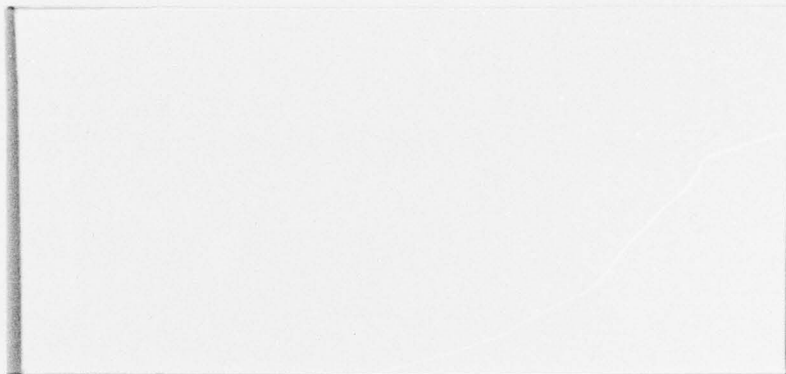


AD No. \_\_\_\_\_  
DDC FILE COPY

ADA 058438

LEVEL *II*

*12*



This document has been approved  
for public release and sale; its  
distribution is unlimited.

**NORTHROP**

Research and Technology Center

78 08 31 043

ADA 058438

AD No. \_\_\_\_\_  
DDC FILE COPY

**LEVEL II**

NRTC 77-15R



UV GAS LASER INVESTIGATIONS  
FINAL TECHNICAL REPORT

Prepared by

W. H. Long, Jr., R. S. Bradford, Jr.,  
J. B. West, and M. L. Bhaumik

Contract N00014-72-C-0456

Sponsored by

ADVANCED RESEARCH PROJECTS AGENCY  
ARPA Order 1807

Monitored by

OFFICE OF NAVAL RESEARCH  
Code 421

NORTHROP CORPORATION  
Northrop Research and Technology Center  
One Research Park  
Palos Verdes Peninsula, California 90274  
Telephone: (213) 377-4811

78 08 31 043

UNCLASSIFIED

SECURITY CLASSIFICATION OF THIS PAGE (When Data Entered)

REPORT DOCUMENTATION PAGE		READ INSTRUCTIONS BEFORE COMPLETING FORM
1. REPORT NUMBER NRTC-77-15R	2. GOVT ACCESSION NO.	3. RECIPIENT'S CATALOG NUMBER
4. TITLE (and Subtitle) UV GAS LASER INVESTIGATIONS,	5. TYPE OF REPORT & PERIOD COVERED Final Technical Report, 15 Apr 1972-30 Mar 1977	
7. AUTHOR(s) W. H. Long, Jr., R. S. Bradford, Jr., J. B. West, and M. L. Bhaumik	6. PERFORMING ORG. REPORT NUMBER NRTC 77-15R	
9. PERFORMING ORGANIZATION NAME AND ADDRESS Northrop Research and Technology Center One Research Park Palos Verdes Peninsula, California 90274	8. CONTRACT OR GRANT NUMBER(s) N00014-72-C-0456	
11. CONTROLLING OFFICE NAME AND ADDRESS Advanced Research Projects Agency 1400 Wilson Blvd. Arlington, Virginia 22209	10. PROGRAM ELEMENT, PROJECT, TASK AREA & WORK UNIT NUMBERS ARPA Order No. 1807	
14. MONITORING AGENCY NAME & ADDRESS (if different from Controlling Office) Office of Naval Research Department of the Navy Arlington, Virginia 22217	12. REPORT DATE	
	13. NUMBER OF PAGES 94	
	15. SECURITY CLASS. (of this report) Unclassified	
	15a. DECLASSIFICATION/DOWNGRADING SCHEDULE	
16. DISTRIBUTION STATEMENT (of this Report) Distribution of this document is unlimited (12) 101p.		
17. DISTRIBUTION STATEMENT (of the abstract entered in Block 20, if different from Report) None		
18. SUPPLEMENTARY NOTES None		
19. KEY WORDS (Continue on reverse side if necessary and identify by block number) Excimer Laser KrF* E-Beam Sustained Discharge High Power Ultraviolet Laser		
20. ABSTRACT (Continue on reverse side if necessary and identify by block number) An experimental and theoretical investigation of rare-gas halide lasers is described. Experiments were conducted in a coaxial, e-beam pumped device and in a transverse, e-beam sustained discharge. Highest laser energy extraction from KrF in the coaxial geometry was 33 J per liter at 12% efficiency. In the transverse device, 29 J per liter was obtained at 11% efficiency. Results are also reported for XeF, XeCl, and Ar-15. Comprehensive theoretical modeling was performed, including electron and molecular kinetics and optical extraction. Considerations for scaling to higher powers are discussed.		

DD FORM 1 JAN 73 1473 EDITION OF 1 NOV 65 IS OBSOLETE

UNCLASSIFIED

i SECURITY CLASSIFICATION OF THIS PAGE (When Data Entered)

407696

LB

UV GAS LASER INVESTIGATIONS

ARPA Order Number:	1807
Program Code Number:	6E20
Contract Number:	N00014-72-C-0456
Principal Investigator and Telephone Number:	Dr. M. L. Bhaumik (213) 377-4811
Name of Contractor:	Northrop Corporation Northrop Research and Technology Center
Scientific Officer:	Director, Physics Programs Physical Sciences Division Office of Naval Research Department of the Navy 800 North Quincy Street Arlington, Virginia 22217
Effective Date of Contract:	15 April 1972 through 30 March 1977
Amount of Contract:	\$1, 201, 345
Sponsored by:	Advanced Research Projects Agency ARPA Order No. 1807

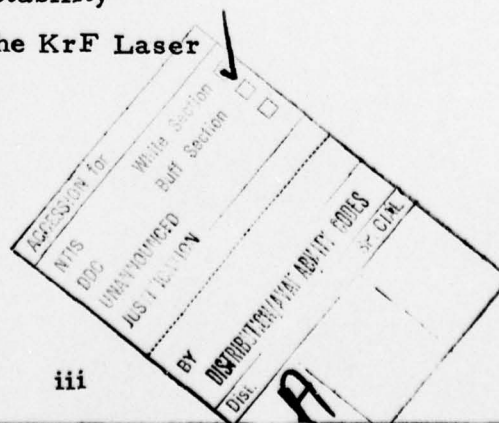
Reproduction in whole or in part is permitted for any purpose of the United States Government.

The views and conclusions contained in this document are those of the authors and should not be interpreted as necessarily representing the official policies, either expressed or implied, of the Advanced Research Projects Agency or the United States Government.



TABLE OF CONTENTS

1.0	SUMMARY	1
2.0	INTRODUCTION	2
3.0	SMALL SCALE EXPERIMENTS	3
3.1	Coaxial E-Beam Pumped Laser	7
3.1.1	Electron Gun	7
3.1.2	Diagnostics	10
3.1.3	Energy Deposition	19
3.1.4	Laser Experiments	21
3.2	E-Beam Sustained Discharge Laser	25
3.2.1	Apparatus	25
3.2.2	Diagnostics	31
3.2.3	Laser Experiments	32
3.3	Additional Laser Discharge Candidates	40
3.3.1	Xenon Halide Lasers	40
3.3.2	Ar-I <sub>2</sub> Transfer Laser	45
4.0	ANALYTICAL MODELING	52
4.1	Electron Kinetics in the KrF Laser	52
4.2	KrF Kinetics	60
4.3	Optical Resonator	64
5.0	SCALING CONSIDERATIONS	70
5.1	Discharge Stability	70
5.2	Scaling of the KrF Laser	77
6.0	CONCLUSIONS	92
7.0	REFERENCES	93



## 1.0 SUMMARY

As a continuing effort to develop efficient new short wavelength lasers based on efficient energy deposition in rare gases, an intensive investigation of the rare gas halide lasers was undertaken. Significant advances were made in understanding the mechanisms and demonstrating the capabilities of this type of lasers. The results clearly demonstrated that the rare gas halides represent a major breakthrough in the search for efficient uv-visible lasers. The most important results are summarized below:

1. Using coaxial e-beam pumping of krypton fluoride (KrF), laser energy extraction of 33 J per liter was demonstrated with an efficiency of 12% based on energy deposited into the gas.
2. Efficient discharge pumping of the KrF laser was demonstrated by achieving a discharge efficiency of 17% in an e-beam sustained discharge device. The overall efficiency in this device due to both e-beam and discharge pumping was 11%, with an output of 27 J/liter.
3. Moderately efficient laser oscillations were also obtained from XeF, XeCl, Ar-I<sub>2</sub>, using e-beam pumping, although KrF was by far the most efficient candidate.
4. Comprehensive kinetic modeling was performed, including electron and molecular kinetics, as well as optical extraction. Results were compared with experimental data for a more thorough understanding of the laser processes.
5. Extensive analyses were carried out to determine the criteria for scaling and discharge stability. The results indicate that specific energy as high as 40 J/liter with efficiencies approaching 10% should be achievable in a scalable e-beam sustained discharge excited KrF laser.

## 2.0 INTRODUCTION

Many important applications requiring visible and shorter wavelength lasers have not been possible due to a distinct lack of efficient, high power lasers in this spectral region. Recently some significant advances have been made which promise to change this situation. The discovery of rare gas excimer and rare gas transfer lasers has provided, for the first time, the most efficient and powerful sources of radiation in the uv region. This is primarily due to the fact that electrical energy can be deposited very efficiently into the rare gas excited states by e-beam or discharge pumping.

The first lasers of this type were the pure rare gas excimers such as  $\text{Xe}_2^*$ . The efficiency of these lasers, however, appears to be limited by processes like photoionization and also by the lack of low loss mirrors. Attempts were then made to utilize the efficient energy deposition in rare gases by subsequent energy transfer to a desirable laser molecule. These efforts led to the  $\text{Ar-N}_2$  lasers. Ultimately, the most efficient rare gas-based lasers have turned out to be the rare gas halide lasers where, instead of energy transfer, the excited rare gas atom undergoes a chemical reaction with the halogens, much like the alkali halides, to form an excimer.

The first rare gas halide lasers were  $\text{XeF}^{1,2}$  (350 nm),  $\text{XeCl}^3$  (308 nm), and  $\text{XeBr}^{4,5}$  (282 nm). Shortly after the discovery of the xenon halide lasers, the  $\text{Ar-I}_2$  (342 nm) transfer laser<sup>6,7</sup> was reported. Subsequent laser experiments with other rare gas halides resulted in the development of the  $\text{KrF}^{3,8}$  laser which is still unsurpassed by any other uv laser in energy output and efficiency. Northrop, under DARPA/ONR sponsorship, has played a key role in the achievement of high energy, high efficiency lasers of this type. The details of these investigations are presented in the following sections, with an emphasis on the most promising KrF laser.



### 3.0 SMALL SCALE EXPERIMENTS

Initial experiments performed by Northrop<sup>8</sup> on KrF consisted of a transverse e-beam pumped mixture of Ar, Kr and  $\text{NF}_3$  using a Physics International Pulserad 110A electron gun which provides a 1 MeV, 20 kA, 20 ns,  $2 \times 10 \text{ cm}^2$  e-beam pulse. The beam entered the side of the 2 cm diameter x 10 cm long optical volume through a  $2.5 \times 10^{-3}$  cm thick titanium foil window, transverse to the optical axis. The optical cavity was composed of 99% and 80% reflecting dielectric mirrors. The active optical volume was  $30 \text{ cm}^3$ . An average current density of  $350 \text{ A/cm}^2$  was measured with a Faraday cup at the foil window as well as 2 cm into the gas. From an e-beam pumped mixture of Ar, Kr and  $\text{NF}_3$  (1300:130:1) at 3.4 atm total pressure, laser output energy was measured to be 100 mJ in a 10 ns (FWHM) pulse. The spectra of both spontaneous and laser emission were photographed with a SPEX 1800 1 m Czerny-Turner spectrograph having a dispersion of 1 nm/mm and are shown in Figure 1.

Spectra of the rare gas halides such as KrF arise<sup>9</sup> from transitions originating at a coulombic upper electronic state and terminating on a repulsive or weakly bound ground state. An energy level diagram is shown in Figure 2. The absence of any sharp structure in the KrF emission spectrum indicates that the transition is of bound-free type. Furthermore, the narrow width (4 nm) of the emission band is understandable in terms of transitions terminating in a relatively flat portion of the repulsive potential curve. The slight intensity alteration appearing as two bands may be the result of some absorption. Due to a large degree of vibrational relaxation at high pressures, emission is expected primarily from  $v' = 0$  of the upper state. A very faint band is also visible towards the short wavelength side separated by nearly  $113 \text{ cm}^{-1}$ . This separation agrees closely with vibrational level spacings of the upper state ( $310 \text{ cm}^{-1}$ ) estimated by Tellinghuisen.<sup>10</sup>



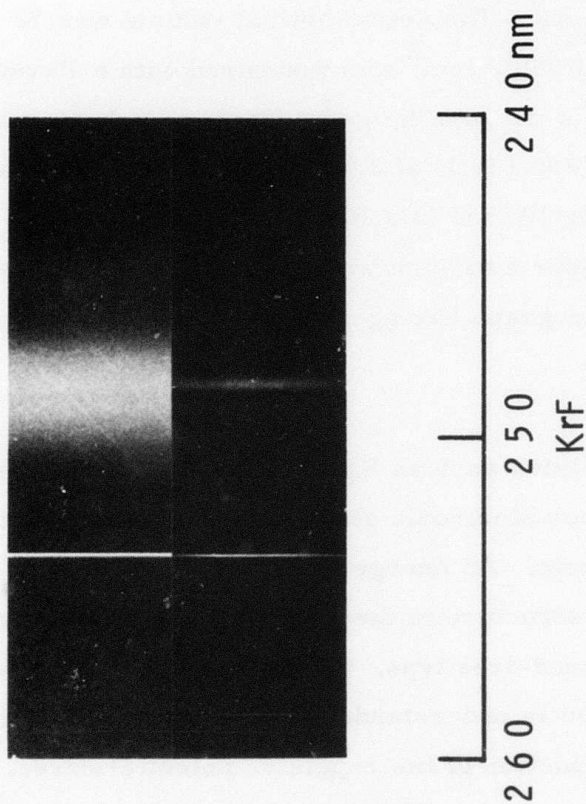


Figure 1. (a) Emission spectrum of KrF from a mixture of 2 Torr  $\text{NF}_3$  and 3.4 atm Ar with 10% Kr obtained by electron-beam pumping. (b) Laser spectrum of the same mixture. The intensity has been attenuated by a factor of  $10^4$  to prevent film saturation.

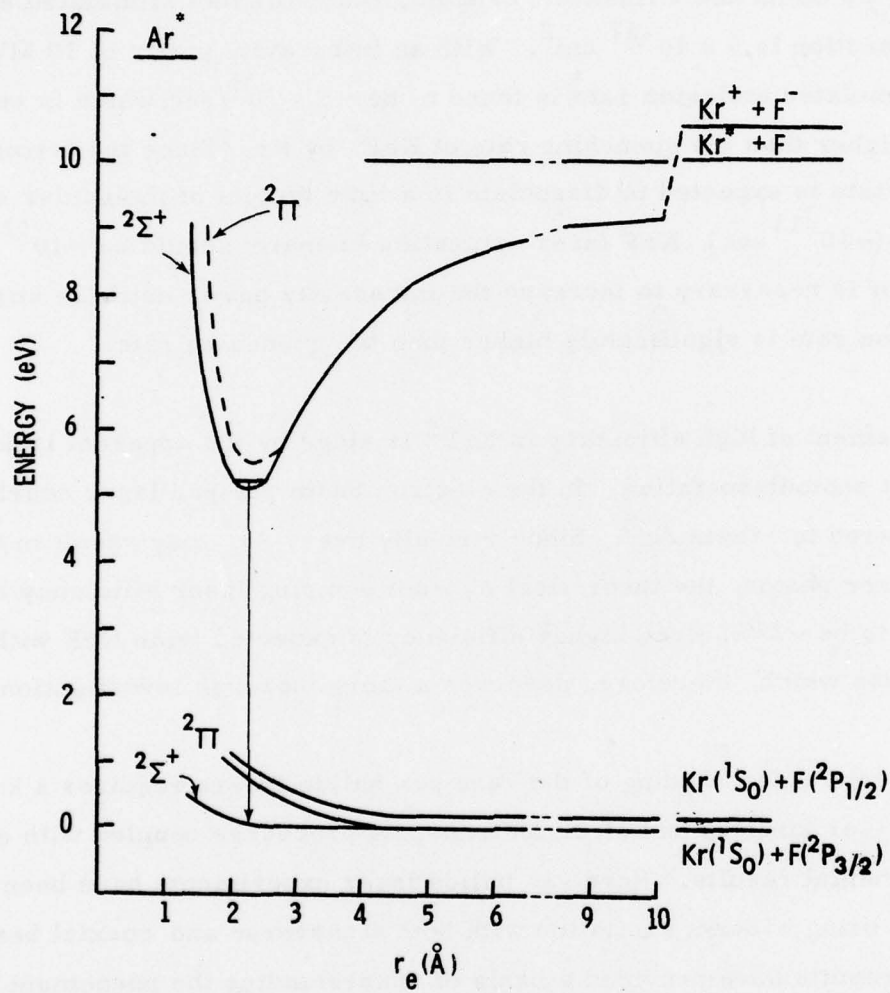


Figure 2. Potential Energy Diagram for KrF

The radiative lifetime of  $\text{KrF}^*$  is expected to be similar to that measured by Searles and Hart<sup>4</sup> for  $\text{XeBr}$  ( $\sim 20$  ns) and by Eden and Searles<sup>11</sup> for  $\text{XeF}$  ( $\sim 17$  ns). Dunning and Hay<sup>12</sup> have performed ab initio calculations on the electronic states of  $\text{KrF}$ . The calculated lifetime was found to be 6.5 ns. Taking  $t = 20$  ns and a linewidth of 4 nm, the estimated stimulated emission cross section is  $5 \times 10^{-17} \text{ cm}^2$ . With an intracavity power of  $10 \text{ MW/cm}^2$ , the stimulated emission rate is found to be  $\sim 5 \times 10^8 / \text{sec}$ , which is estimated to be higher than the quenching rate of  $\text{KrF}^*$  by Kr. Since the terminal laser state is expected to dissociate in a time typical of molecular vibrational period ( $\sim 10^{-13}$  sec),  $\text{KrF}$  laser saturation intensity should be  $\sim 10^{12} \text{ W/cm}^2$ . Thus, it is necessary to increase the intracavity power until the stimulated emission rate is significantly higher than the quenching rate.

Achievement of high efficiency in  $\text{KrF}^*$  is aided by the apparent lack of significant photodissociation. In the electron beam pumped laser nearly 20 eV is required to create  $\text{Ar}^*$ . Since virtually every  $\text{Ar}^*$  may result in a 5 eV  $\text{KrF}$  laser photon, the theoretical e-beam pumping laser efficiency is expected to be  $\sim 25\%$ . Even higher efficiency is expected from  $\text{KrF}$  with discharge excitation which, therefore, deserves a more thorough investigation.

A complete understanding of the rare gas halide lasers requires a knowledge of the laser kinetics and electron transport processes coupled with extensive experimental results. Rare gas halide laser experiments have been performed using e-beam excitation with both transverse and coaxial beams. These results have provided a basis of understanding the phenomenology of the  $\text{KrF}$  system and are presented in Sections 3.1 and 3.2. Additional laser candidates are discussed in Section 3.3.

For discharge excitation, optimum discharge parameters and power partitioning must be determined to predict the ultimate performance of this

class of lasers. Northrop has developed an electron transport code to optimize these parameters. The theoretical basis of the code is discussed in Section 4.1. Section 4.2 presents a summary of KrF kinetics and Section 4.3 analyzes the optical resonator with distributed absorption.

### 3.1 Coaxial E-Beam Pumped Laser

This section describes the experimental results from a table-top sized, coaxially excited, KrF laser which delivered 3.3 J of energy from a 0.10 liter volume with 12% efficiency. The device is pictured in Figure 3. The Marx driver is mounted on top of the vacuum envelope enclosing the gun diode. The system is pumped with a 6-inch water cooled diffusion pump and a two-stage mechanical forepump.

#### 3.1.1 Electron Gun

The electron gun produces a 300-400 keV beam of electrons at  $20\text{-}40\text{ A/cm}^2$  directed radially inward on a cylindrical foil. The overall dimensions of the diode-driver combination are 178 cm x 50 cm x 50 cm. This consists of a 128 cm diameter by 38 cm long cylinder housing, the Marx driver circuitry, and a 50 cm x 50 cm x 50 cm lead box enclosing the gun diode section.

##### 3.1.1.1 Diode

The anode is made from 1 mil titanium foil rolled into a 2.54 cm diameter cylinder and laser-welded along the seam (Figure 4). The cathode consists of 8 longitudinal blades, each 20 cm long, equally spaced around the anode at a distance of 3.3 cm. These blades were mounted on a 10 cm diameter cylinder with a sidearm leading to the Marx driver. The anode is sealed on either end to a stainless-steel flange holding a laser mirror. The pressure inside the anode during the laser experiments was typically 35-45 psi and



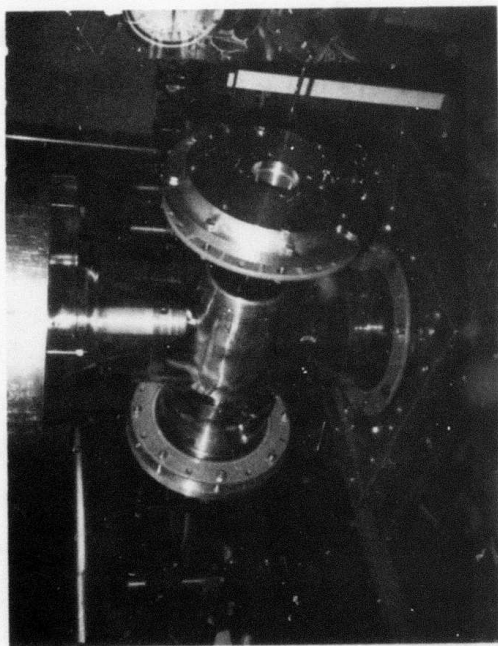
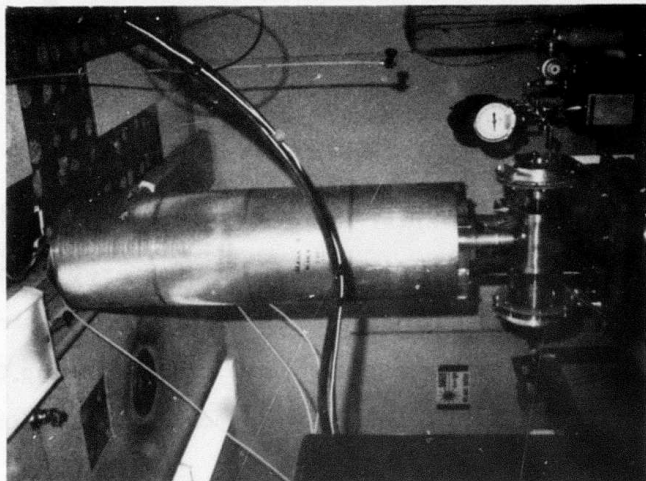


Figure 3. Photographs of the NRTC Coaxial E-Beam Pumped Laser

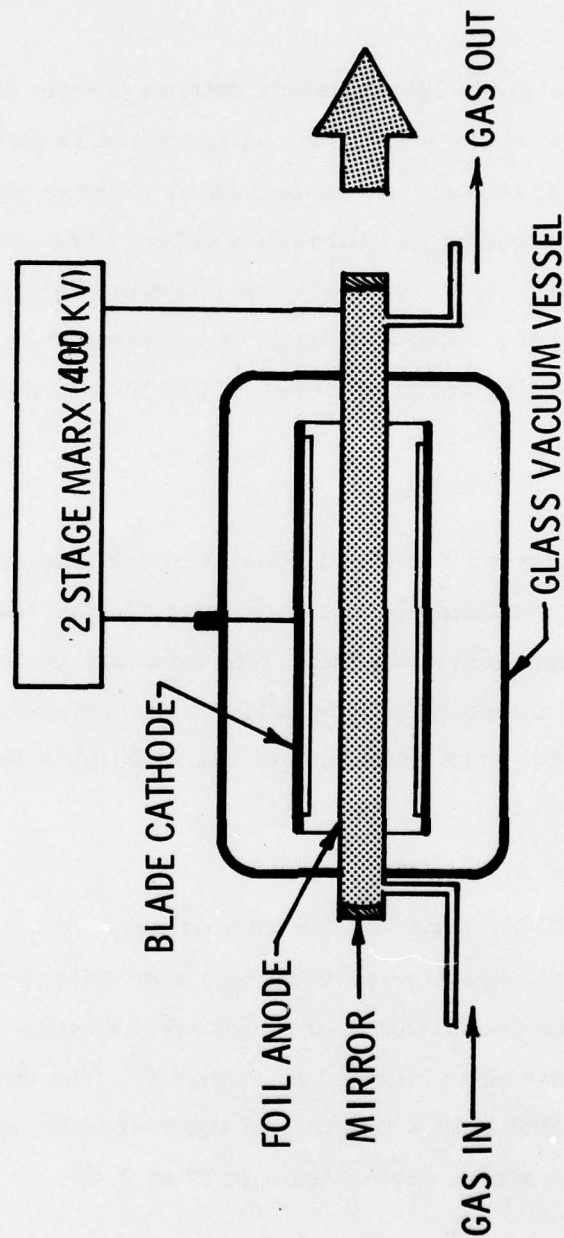


Figure 4. Schematic of the Coaxial Electron Gun and Laser Components

was tested under static conditions to 100 psi. The base pressure in the diode section is maintained at about  $2 \times 10^{-6}$  Torr.

#### 3.1.1.2 Driver

The gun is driven by a two-stage Marx circuit with an energy storage of 400 J at a charging voltage of 200 kV. The configuration is pictured in Figure 5. Two 0.01  $\mu$ F capacitors are connected by a spark gap which is triggered by exhausting the buffer gas through a valve. The main spark gap then fires automatically, applying twice the charging voltage to the cathode. The rise time of the cathode voltage is between 10 ns and 25 ns from zero to peak for charging voltages between 150 kV and 200 kV.

#### 3.1.2 Diagnostics

The diagnostics for the electron gun itself consist of a  $\dot{B}$  loop and voltage divider to indicate the current and voltage waveforms in the Marx circuit and a current probe and pressure transducers to measure the current density and pressure rise inside the anode. The signals were monitored simultaneously on HP Model 454A oscilloscopes with 20 MHz bandwidth.

##### 3.1.2.1 $\dot{B}$ Loop

The  $\dot{B}$  loop consists of a single turn of wire located near the grounded terminal of the lower Marx capacitor (Figure 5). The voltage measured across a 50 $\Omega$  terminator is proportional to the current flowing in the driver circuit. Typical waveforms are indicated in Figure 6. The damped sinusoidal behavior indicates that only a fraction of the stored energy is dissipated in the diode. This fraction varies from 0.79 to 0.85.

##### 3.1.2.2 Voltage Divider

A schematic of the voltage divider used to measure cathode voltage is shown in Figure 7. The 1.2 k $\Omega$  variable resistor is a plastic tube filled with copper

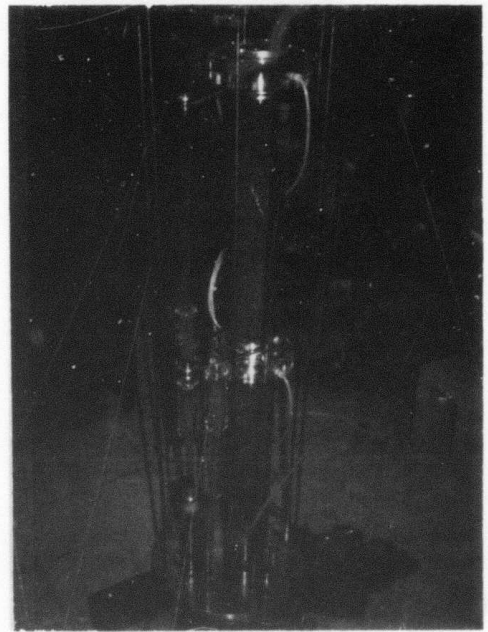
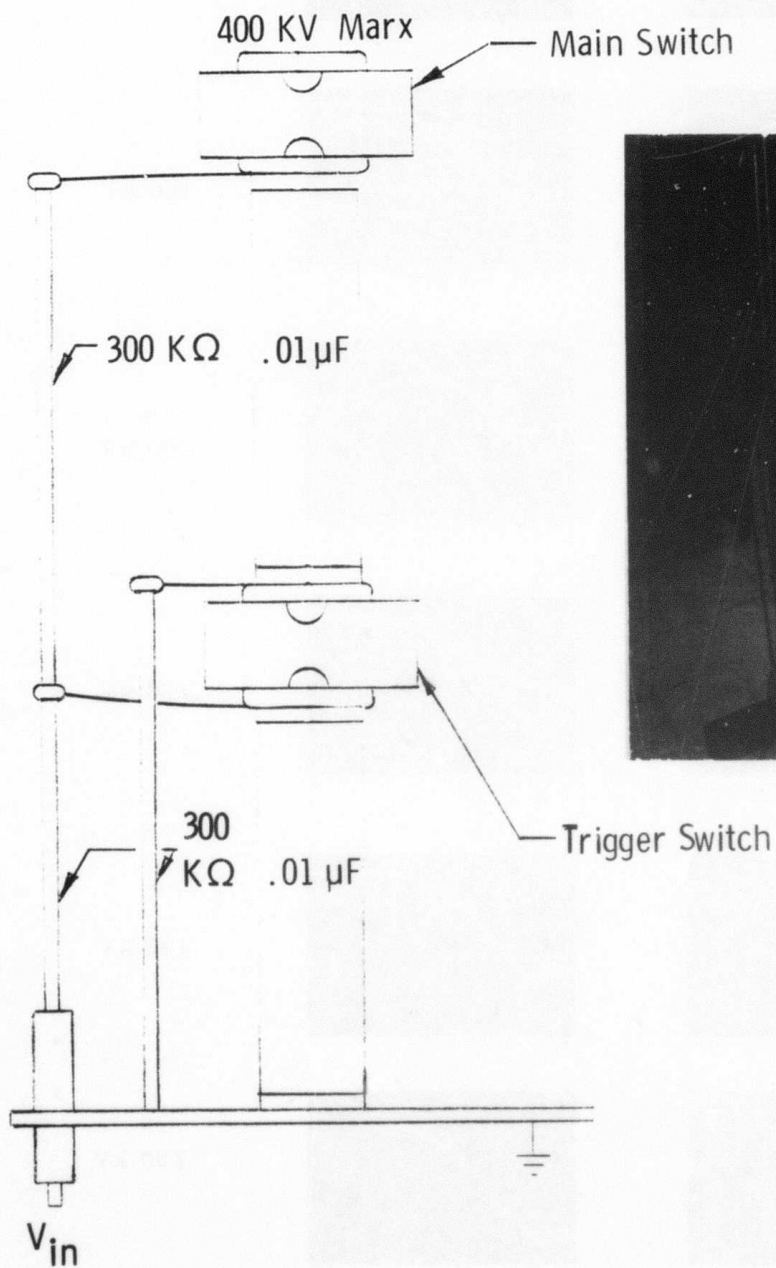


Figure 5. Two-Stage Marx Circuit Driver



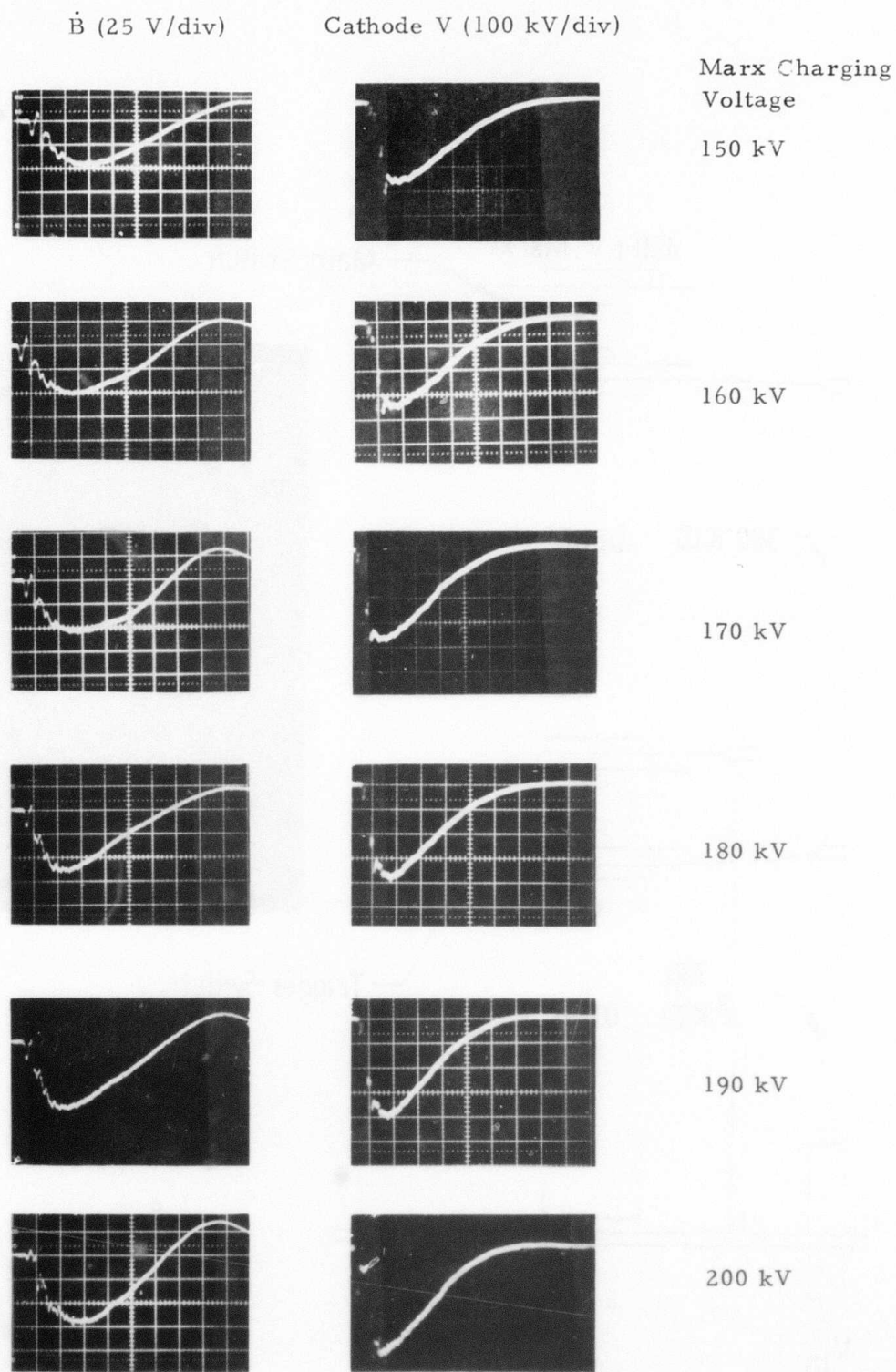


Figure 6. Current and Voltage Waveforms for the Coaxial Electron Gun (50 ns/div)

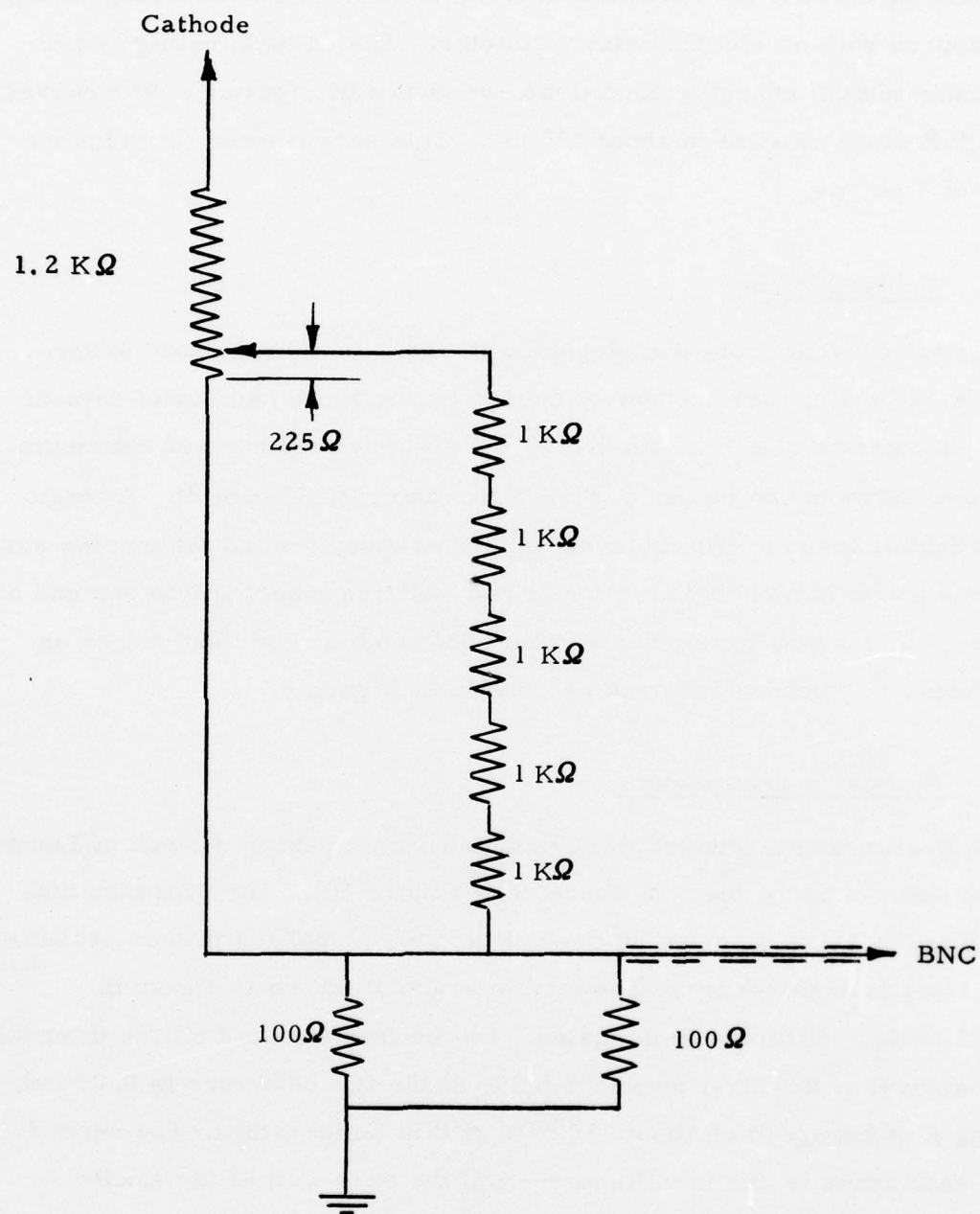


Figure 7. Schematic of the Cathode Voltage Divider

sulfate . The fixed resistors are carbon. The divider was pulse-calibrated by discharging a 0.001  $\mu$ F capacitor charged to 24 kV. The charging voltage was measured with an electrostatic voltmeter. The cathode voltage waveforms under typical charging conditions are shown in Figure 6. The curves indicate full diode closure in about 450 ns . This corresponds to a closure velocity of 7 cm/ $\mu$ s.

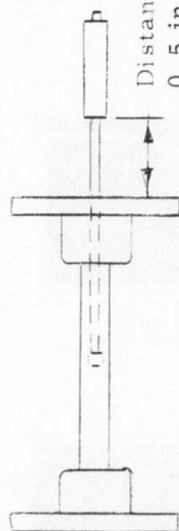
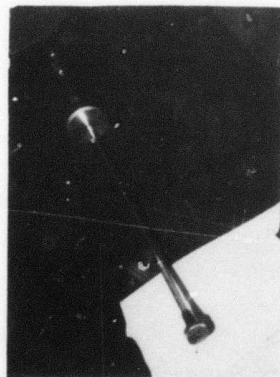
#### 3.1.2.3 Current Probe

A cylindrical current probe was designed in order to average out the azimuthal variations in current density caused by the finite number of cathode blades. It consists of a 0.15 cm x 2.13 cm diameter cylinder of aluminum sandwiched between two pieces of dielectric material (Figure 8). A single layer of Scotch brand magic mending tape is wrapped around the outside surface. The probe is mounted on a metal rod which is inserted into one end of the anode. The signal is terminated in a 50  $\Omega$  resistor and read out on an oscilloscope. Typical waveforms are shown in Figure 9.

#### 3.1.2.4 Pressure Transducers

A pair of pressure transducers were mounted 3 cm apart in a block of Lucite affixed to one end of the high-pressure cell (Figure 10). The pressure diaphragm amplifiers were set to 50 psi/volt and the signal fed into an oscilloscope. A representative trace obtained in argon at 35 psi is shown in Figure 11 on four different time scales. On the fast scale, the time interval between arrival of the first pressure pulse at the two detectors is 0.09 ms, indicating a sound speed of about 330 m/s at this temperature. The second pulse in each trace is due to reflection from the back wall of the Lucite cylinder.

The 1 ms/div time scale indicates a series of double peaks, with a 3.5 ms periodicity. The major peaks represent the two compression waves originating from opposite ends of the excitation region. The 5 ms/div time



Distance in inches  
0.5 in. to 8 in. referred to  
in photographs.

Current Probe Material: Aluminum

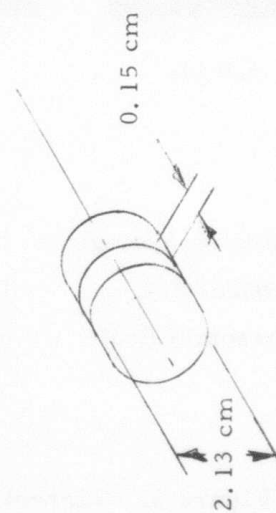
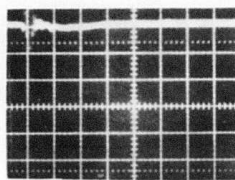
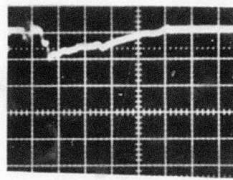


Figure 8. Specially Designed Cylindrical Current Probe

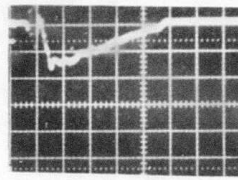




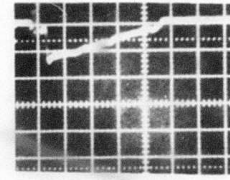
.5 in.



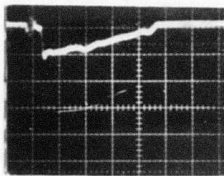
.75 in.



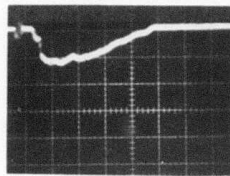
1.0 in.



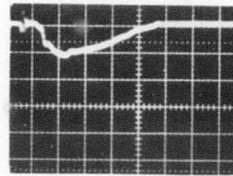
1.25 in.



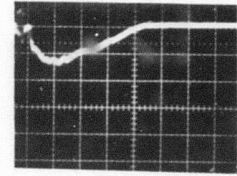
1.5 in.



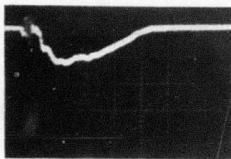
2.0 in.



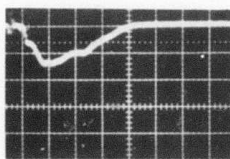
3.0 in.



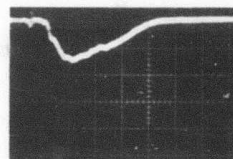
4.0 in.



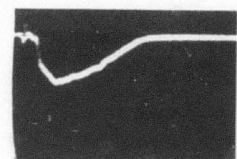
5.0 in.



6.0 in.



7.0 in.



8.0 in.

Charging Voltage = 150 kV  
Vertical Scale =  $18 \text{ A/cm}^2/\text{div}$   
Horizontal Scale = 50 ns/div

Figure 9. Current Probe Waveforms at Several Axial Positions

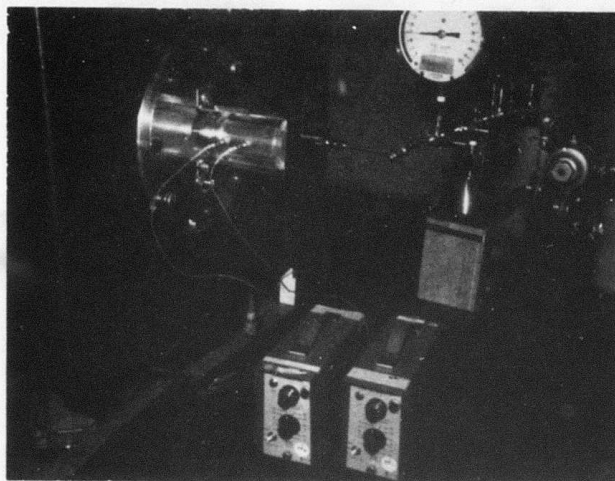
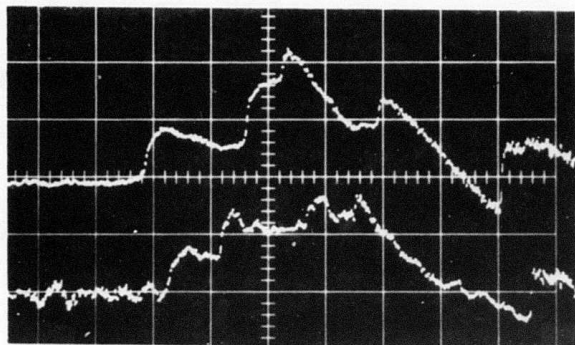
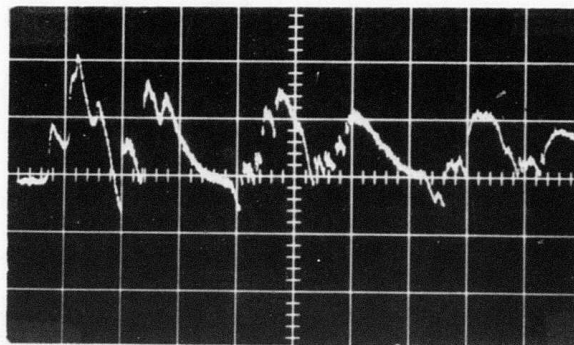


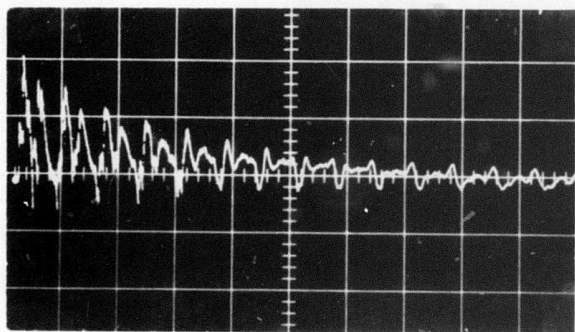
Figure 10. Pressure Transducers Mounted on the Coaxial Electron Gun



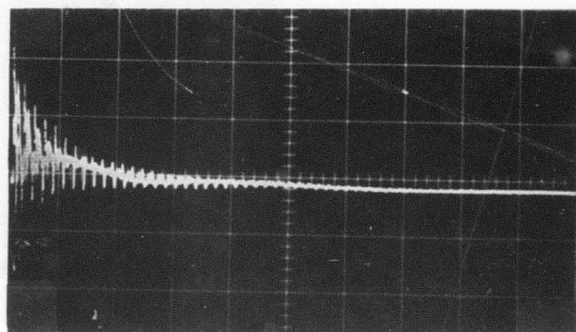
0.2 ms/div



1. ms/div



5. ms/div



20 ms/div

Charging Voltage = 150 kV  
 Pressure = 35 psi  
 Vertical Scale = 0.1 V/div

Figure 11. Pressure Waves in the Coaxial Gun on Several Different Time Scales

scale shows the gradual rise and fall of the baseline pressure as hot gas moves into the measurement region. The slowest scale shows the gradual attenuation of the pressure waves as they cycle around inside the high-pressure cell.

### 3.1.3 Energy Deposition

In order to determine the laser efficiency, it is necessary to know how much of the energy stored in the Marx bank is actually deposited in the gas. Two methods were employed: (1) The power density was inferred from the measured current density and the known stopping power of the laser mixture, and then integrated over the pulselength and excited volume. (2) The pressure rise inside the anode was determined from the measured strength of the compression wave leaving the excitation region and then translated into an energy density.

#### 3.1.3.1 Current Density Measurements

The e-beam current density as a function of axial position is shown in Figure 12 for two different charging voltages. The peaks at each end of the excitation region are due to pinching of the electron beam. The linear stopping power of a 5% Kr 95% Ar mixture for 300 keV electrons is 2.94 keV/cm/atm. For 400 keV electrons it is 2.70 keV/cm/atm. The measurements and Monte Carlo calculations carried out at Livermore indicate that the effective stopping power at the foil is actually about 3 times this value due to scattering in the gas. From the foil, the energy deposition falls off linearly at first with a zero intercept at about 0.62 of the initial residual range. The average stopping power is found by integrating this function over the circular cross section of the anode. The energy deposition is equal to the average stopping power times the average current density times the pulsewidth (140 ns). Typical values are shown in Table I as a function of total pressure and charging voltage.



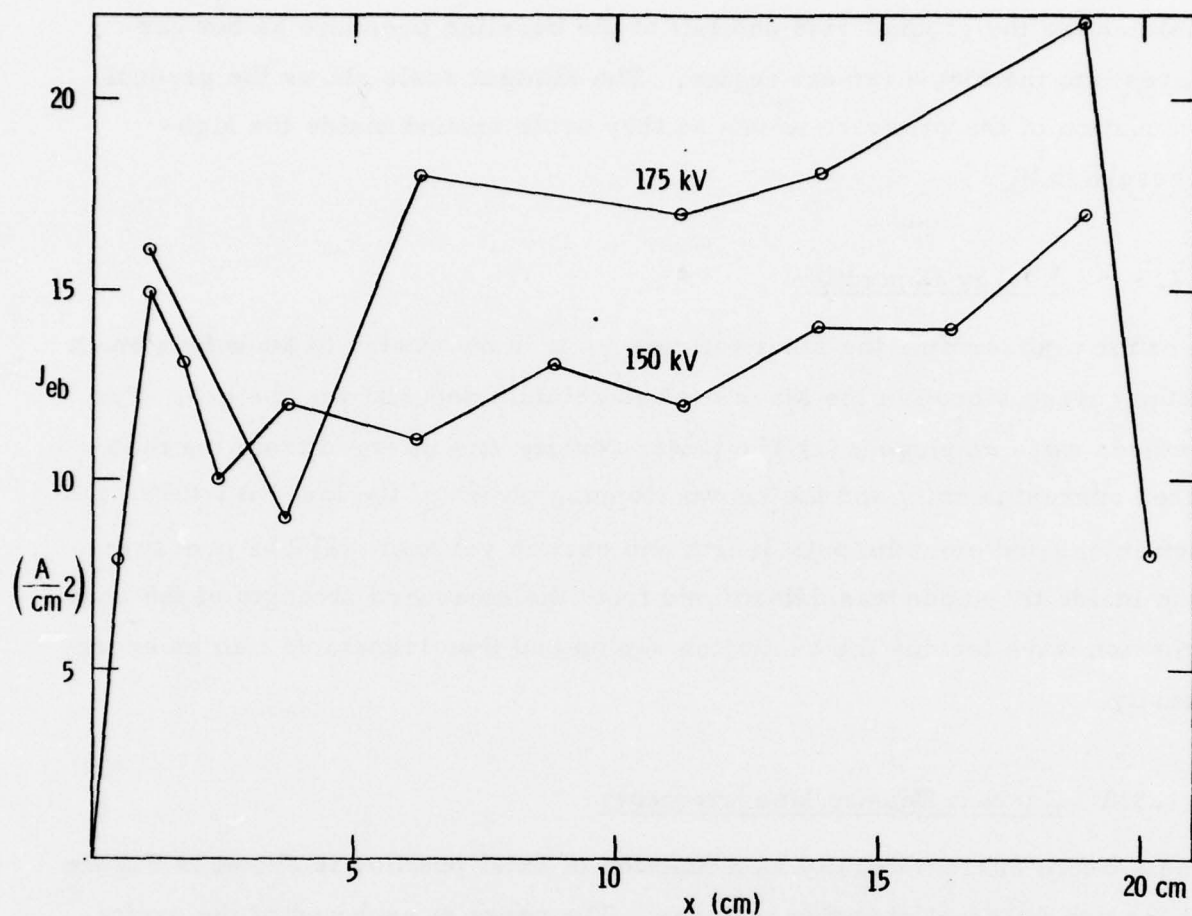


Figure 12. Current Density Through the Anode Foil

Table I. Energy Deposition in the Coaxial E-Beam Laser

pressure	Charging Voltage		
	150 kV	175 kV	200 kV
35 psi	146 J/l	185 J/l	223 J/l
45 psi	179 J/l	229 J/l	278 J/l
current density $\bar{J}$	14 A/cm <sup>2</sup>	18 A/cm <sup>2</sup>	22 A/cm <sup>2</sup>

#### 3.1.3.2 Pressure Measurements

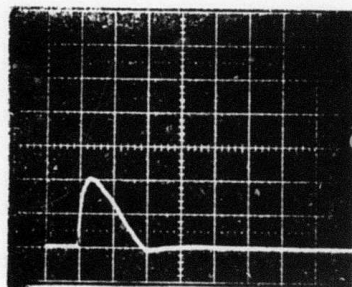
The strength of the compression wave reaching the first detector is related to the pressure rise in the excitation region,  $\Delta p$ , by the basic shock tube equation. For the weak shocks experienced in this experiment, the pressure rise across the first compression wave was roughly equal to  $\Delta p/2$ . For the case shown in Figure 11, we get  $\Delta p = 10$  psi. The thermal energy density in argon at atmospheric pressure is  $152 \text{ J/l}$ , so that a pressure rise from 35 psi to 45 psi corresponds to  $103 \text{ J/l}$  of thermal energy deposited. Since the fluorescence efficiency of argon is about 37% under these pumping conditions, the total energy deposited by the e-beam should be  $163 \text{ J/l}$ . This is in reasonable agreement with the value derived from the current density measurements.

#### 3.1.4 Laser Experiments

For the laser experiments, an optical cavity was formed with two partially reflecting mirrors placed at either end of the anode cylinder in direct contact with the laser gas. Special fluorine resistant coatings were necessary to withstand the harsh environment. An alternative arrangement with AR windows and external mirrors was not nearly as successful in terms of energy extraction.

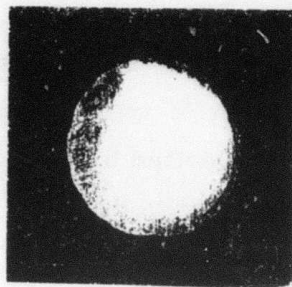
The optical output was measured with a pair of integrating pyroelectric joulemeters. A beam splitter was used to divert 10% of the output from one end into a fast planar photodiode to show the temporal behavior of the laser pulse (Figure 13(a)). The laser pulsewidth from KrF was typically 125 ns with an e-beam current pulsewidth of 140 ns. The laser burn pattern (Figure 13(b)) indicates that the entire excited volume was lasing. The beam divergence was typically 10 mrad.

(a)



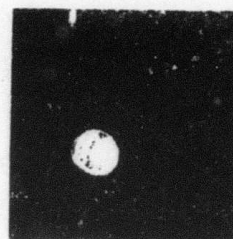
100 ns/div  
10 V/div  
F4115 Photodiode

(b)



Burn Pattern  
 $\approx 1.5 \text{ J}$

(c)



Focused Burn  
Pattern  
 $\approx 1.5 \text{ J}$

Figure 13. Photodiode Trace and Burn Patterns from KrF

#### 3.1.4.1 XeF Results

Experiments on XeF using the coaxial e-gun were carried out using only one gas mixture, 0.4% NF<sub>3</sub>, 10% Xe, 89.6% Ar. No attempt was made to optimize the mix or the total pressure. The charging voltage was 200 kV at 32 psi total pressure. Laser output was 80 mJ in a 90 ns wide pulse.

#### 3.1.4.2 KrF Results

Several mixtures were tested containing argon, krypton, and fluorine over a range of pressures and charging voltages. The output couplers were 50% and 70% reflecting. The results are presented in Table II.

The largest energy extracted from KrF was 3.3 J. This was achieved at 45 psi total pressure in a mixture containing 0.3% F<sub>2</sub>, 4.7% Kr, and 95% Ar. The Marx bank was charged to 200 kV. The estimated energy deposition was (Table I)  $278 \text{ J/l} \times 0.101 \text{ l} = 28 \text{ J}$  for a laser efficiency of 11.9%. Since 400 J was stored in the Marx, the wall-plug efficiency is 0.8%.

In a mix with less fluorine, 0.2%, the maximum energy was 2.55 J at 45 psi and 175 kV charging. In this case the deposited energy was 23 J for a laser efficiency of 11.1%. In the same mix at 35 psi and 175 kV, the best shot was 2.26 J for a 12.1% efficiency. This gas mixture was not tried at 200 kV charging.

The burn pattern in Figure 13 and the current density traces in Figure 12 indicate that the active volume was close to the geometrical value of 0.101 l. Thus, under the best conditions, the laser was operating at 33 J/l with a 12% efficiency based on energy deposited.



Table II. Experimental Data for KrF in the Coaxial E-Gun Laser

Charging Voltage	Total Pressure	Laser Output
$F_2:Kr:Ar = 1:52:1034$		
175 kV	35 psi	0.85 J
175 kV	40 psi	1.13 J
175 kV	45 psi	1.27 J
175 kV	50 psi	1.37 J
$F_2:Kr:Ar = 1:26:517$		
175 kV	35 psi	2.26 J
175 kV	45 psi	2.55 J
$F_2:Kr:Ar = 1:17:345$		
200 kV	45 psi	3.34 J
$F_2:Kr:Ar = 1:13:258$		
200 kV	45 psi	2.38 J

### 3.2 E-Beam Sustained Discharge Laser

An extensive experimental study of KrF was conducted using an e-beam controlled, discharge pumped laser which delivered 3.2 J of energy from a 0.12 l volume with 11% efficiency.

#### 3.2.1 Apparatus

The device is pictured in Figure 14. The overall dimensions of the electron gun and laser plenum are 175 cm x 61 cm x 46 cm. This consists of a 122 cm x 61 cm x 46 cm oil tank housing the Marx circuitry, a 42 cm diameter x 38 cm long lead cylinder enclosing the gun diode, and a 15 cm diameter x 42 cm long cylindrical laser plenum.

The laser plenum is rated at 10 atm and is completely halogen compatible. Only teflon, aluminum and stainless steel are used. Great care has been exercised to assure reproducible concentrations of the halogens within the laser mixture so that accurate experimental data would be obtained. Standard high vacuum practices were followed with the entire gas handling system to guarantee clean laser gases of known concentration.

##### 3.2.1.1 Electron Gun

The cold cathode electron gun has a 22 cm x 4 cm aperture whose normal is perpendicular to the optical axis. A ladder-like structure, supporting a 1 mil titanium foil, acts as the anode. The cathode consists of a single blade mounted on a cylindrical rod. The A-K spacing can be adjusted accurately between 1 cm and 4 cm by turning a threaded shaft.

The gun is driven by a 3-stage Marx circuit with an energy storage of 225 J (or 450 J) at a charging voltage of 100 kV. (The larger energy storage was used in an effort to lengthen the excitation pulse. See Section 3.2.3.) Three 0.015  $\mu$ F (or 0.03  $\mu$ F) capacitors are connected by spark



Figure 14. E-Beam Sustained Discharge Laser

gaps, as shown in Figure 15. The lower gap is exhausted to trigger the circuit and the Marx erects in about 10 ns. The following table summarizes the gun performance:

Electron Beam Cross Section	=	22 cm x 4 cm
Electron Beam Energy	=	300 keV
Transmitted Current Density	=	5-40 A/cm <sup>2</sup>
Pulse Duration	=	150-300 ns

#### 3.2.1.2 Discharge Circuit

The e-gun foil forms the positive discharge electrode while a modified Rogowski-profiled aluminum bar forms the discharge cathode. A diagram of the electrodes and the discharge circuit is shown in Figure 16. Energy stored in the discharge capacitor is switched on to the cathode at the same instant that the e-gun is energized. This synchronization is achieved by triggering the spark gap switch with a signal from the second stage of the Marx circuit (Figure 15).

The discharge capacitor is 0.225  $\mu$ F and can be charged up to 30 kV, for a stored energy of 101 J. The circuit inductance was measured by placing an aluminum block between the electrodes and measuring the ringing frequency. A value of 160 nH was obtained.

#### 3.2.1.3 Optics

The optical cavity is formed by a partial reflector (77%) and a total reflector (98%) mounted 50 cm apart on the ends of the laser plenum (Figure 17). The stable resonator quartz optics also serve as the plenum pressure windows, thereby reducing the absorption losses which would be introduced by separate windows. The laser output is directed through a beam splitter into a Gen-Tec calorimeter which was calibrated at 2.65 V/J. The beam splitter diverts 10% of the output through a series of neutral density filters onto a photodiode to show the temporal behavior of the pulse.



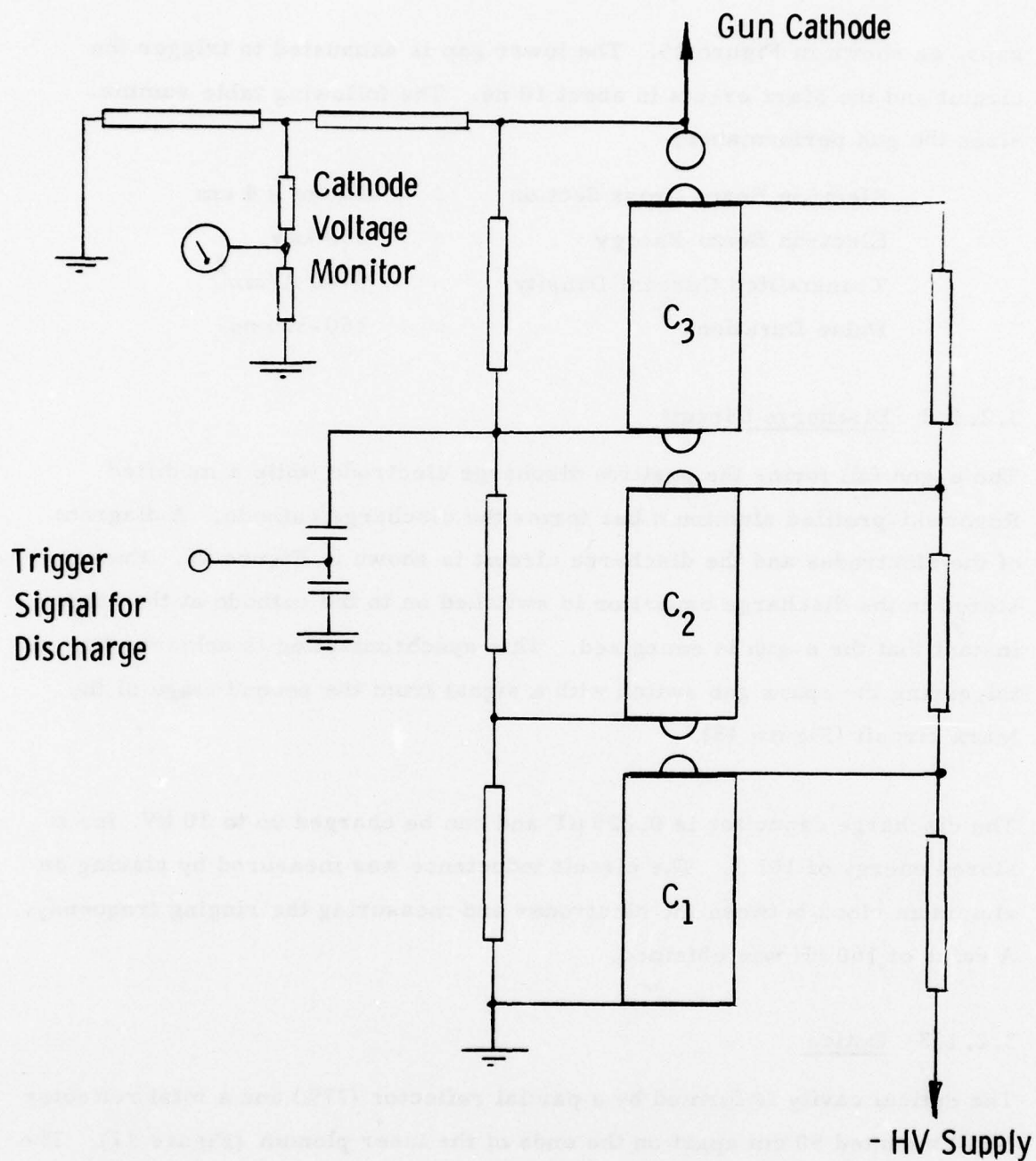
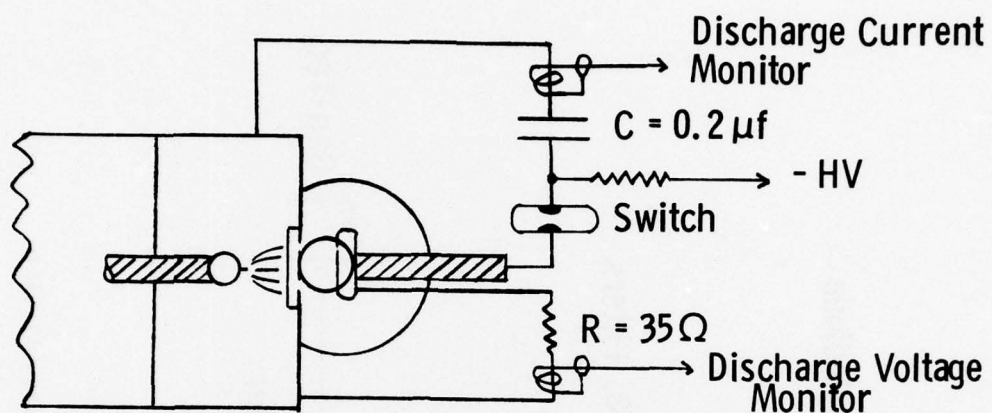


Figure 15. 3-Stage Marx Circuit



Marx Voltage	300 kV
$J_B$	5 - 40 A/cm <sup>2</sup>
Pulselength	250 ns
Extracted Volume	100 - 200 cm <sup>3</sup>

Figure 16. Discharge Circuit and Diagnostics

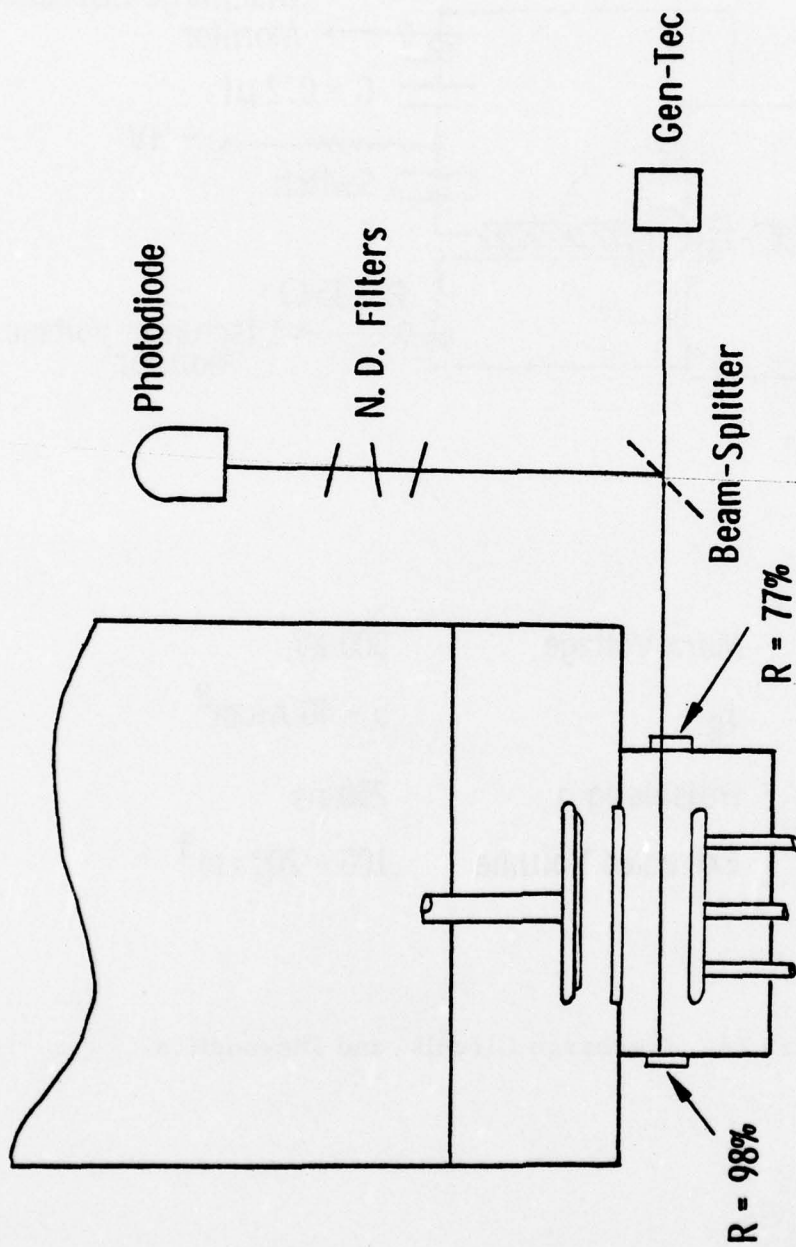


Figure 17. Optical Diagnostics for 0.1 Liter Device

### 3.2.2 Diagnostics

The electrical diagnostics include: (1) a  $\dot{B}$  loop to monitor the Marx current and to trigger the oscilloscopes, (2) a planar Faraday probe to measure transmitted e-beam current density, (3) a low-impedance discharge voltage monitor, and (4) a Pearson coil to measure discharge current. The optical diagnostics consist of a planar photodiode and a Gen-Tec joulemeter. Five oscilloscopes were used to simultaneously record these signals on each shot. The Faraday probe measurements were taken in a separate set of runs.

#### 3.2.2.1 Faraday Probe

The electron beam current density was measured with Faraday probes designed and fabricated at NRTC. Each probe consists of a 0.36 cm diameter copper rod approximately 10 cm long. A 0.63 cm outside diameter stainless steel tube, coaxial with the copper rod, acts as a shield. Insulation between the center rod and shield is provided by a Pyrex tube. The end of the probe is finished by sealing the joints between the copper, stainless steel and Pyrex with HYSOL EPOXIPATCH and lapping flat after the epoxy has hardened. The other end is terminated with a BNC fitting. Signals from the Faraday probes are recorded with an oscilloscope using voltage attenuators, as needed, and a  $50\Omega$  termination. A typical calibration factor for one of these probes is 240 mA/V.

Beam current measurements are usually made in air a few millimeters from the foil. When these probes are used in air, or other such gas, a single layer of Scotch brand magic mending tape is placed over the end. This prevents shorting between the probe and shield caused by the gas plasma.



#### 3.2.2.2 Discharge Current

Total discharge current is measured with a pulse current transformer in the ground return path of the discharge circuit, as shown in Figure 16. These current transformers, manufactured by Pearson Electronics, have a calibration factor of 0.05 V/amp when a 50  $\Omega$  termination is used at the oscilloscope input.

#### 3.2.2.3 Discharge Voltage

Early in the program, discharge voltages were measured using a high impedance resistive voltage divider just outside the feedthroughs to the discharge electrode. This was found to be unsatisfactory due to effects caused by inductive voltage drops at the feedthroughs and stray capacitance. Therefore, an alternative method, shown in Figure 16, was adopted. This technique uses a low resistance (35  $\Omega$ ) ammonium sulfate resistor connected between the discharge electrode and ground. Current through this resistor is measured using the same type of pulse current transformer described above for the discharge current measurement. Ohm's law is then used to calculate the discharge voltage. Since the resistance of the plasma is typically 1  $\Omega$  or less, the additional 35  $\Omega$  resistor connected in parallel has little effect on the discharge.

#### 3.2.3 Laser Experiments

In order to optimize the performance of the KrF laser, a number of experiments were carried out over a wide range of pumping conditions, pressures, and gas mixtures. The specific goals of that investigation were to determine the enhancement due to discharge pumping and to maximize the efficiency and energy extraction from a fixed volume. The results are presented below.

Typical experimental waveforms are shown in Figure 18. (The timing pulse at the right of each oscillogram was used for synchronization of the various

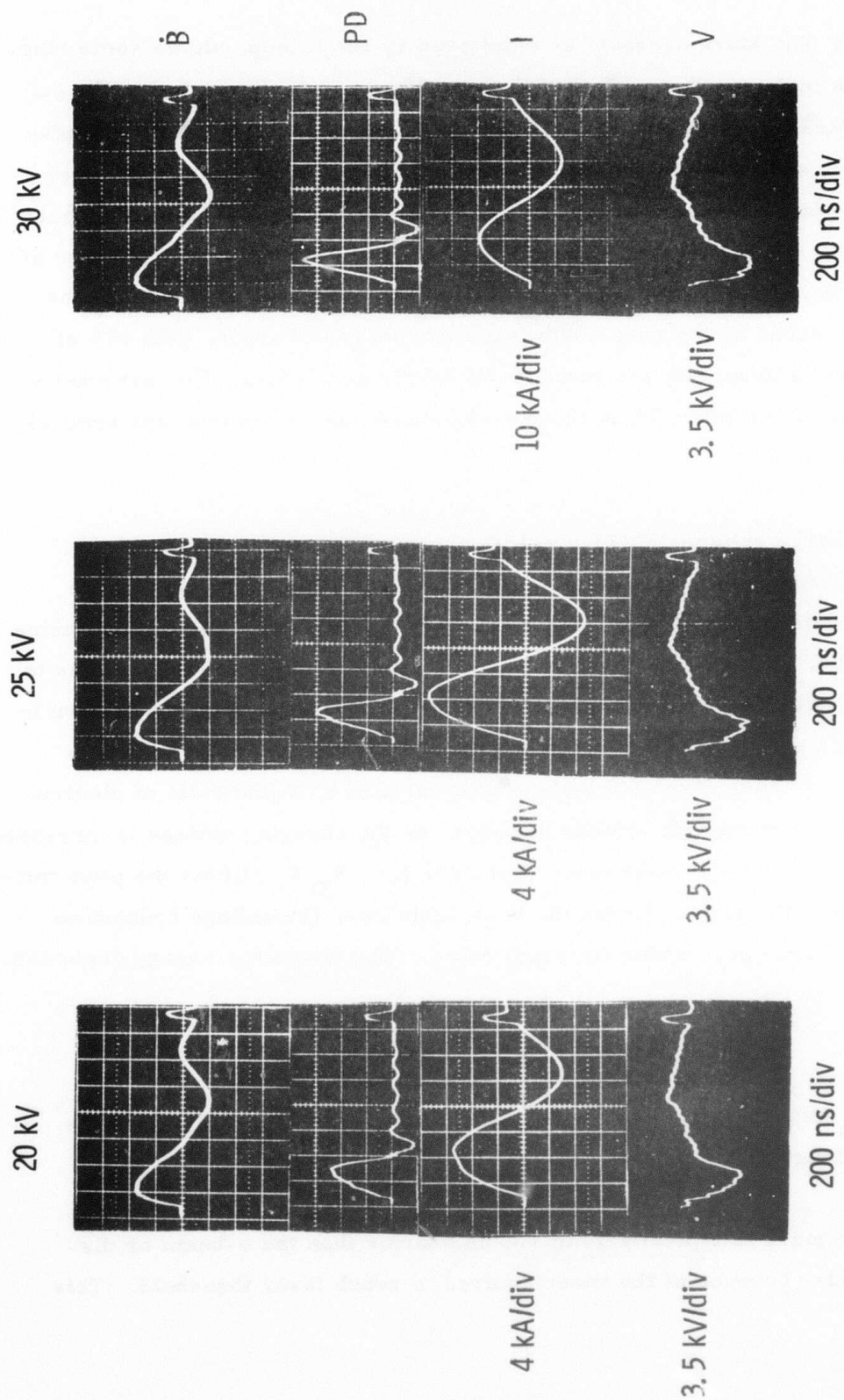


Figure 18. Discharge Current and Voltage Curves as a Function of Discharge Capacitor Charging Voltage  
 $J_B = 17.9 \text{ A/cm}^2$

signals.) The Marx current, as monitored by the  $\dot{B}$  loop, shows some ringing which indicates that not all of the stored energy is dissipated in the gun diode. Measurement of the electron beam current density using a Faraday probe indicates that about 60% of the energy stored in the Marx circuit is delivered to the beam. Of this energy, 10% is absorbed by the foil support structure, 15% of the rest is lost in the foil, and with three atmospheres of argon in a 2 cm electrode gap, about 15% of the energy coming through the foil is absorbed by the gas. With two atmospheres of argon, only 10% of the energy is absorbed; the rest hits the anode and is lost. The net energy deposition is therefore 7% in three atmospheres and 5% in two atmospheres of argon.

The discharge voltage,  $V$  (Figure 18), rises roughly proportional to the discharge current,  $I$ , for the first 200 ns, indicating that the impedance, which is determined by the e-beam current density, is fairly constant during this period. The voltage then drops suddenly while the current continues to rise, signaling a breakdown of the discharge impedance. It will be shown in Section 5.1 that this breakdown is a volume runaway caused by two-step ionization which occurs at a well-defined value of  $E/N$  (the ratio of electric field strength to neutral number density). As the charging voltage is increased, the discharge voltage rises more rapidly ( $\dot{E}(0) = R_D V_0 / L$ ) but the peak voltage remains the same. Under the best conditions, the voltage breakdown occurs near the peak of the first half cycle. The discharge energy deposited in the gas is therefore,

$$\mathcal{E}_d = V_p I_p \tau / 2$$

where  $V_p$  and  $I_p$  are the peak voltage and current, respectively, and  $\tau$  is the pulselength.

The laser pulse is typically 50 to 100 ns shorter than the e-beam or discharge pulse because of the time required to reach laser threshold. This

time is dependent on the current rise times in both the gun and the discharge which are proportional to the charging voltages. The laser pulse terminates sharply with the onset of the ionization instability mentioned previously, even though there is still substantial pumping. This is believed to be due to a rapid rise in the concentration of molecular ions,  $\text{Ar}_2^+$  and  $\text{Kr}_2^+$ , which are strong absorbers at the laser wavelength.

The highest laser output energy of 3.2 J from  $\text{KrF}^*$  was achieved with a gas mixture containing 0.14%  $\text{F}_2$ , 4.5% Kr, and 95.4% Ar at a total pressure of 45 psi. The large Marx capacitors (0.03  $\mu\text{F}$ ) were charged to 100 kV, and the discharge capacitor (0.22  $\mu\text{F}$ ) was charged to 25 kV. The A-K spacing in the gun was 1.75 cm and in the discharge was 2 cm. The output waveforms are shown in Figure 19. The e-beam current density under these conditions was checked before and after the laser shot and indicated 40  $\text{A}/\text{cm}^2$  with a pulselength of 220 ns. The maximum discharge voltage and current were 4.5 kV and 20 kA respectively. The 3.2 J output came in a pulse 160 ns wide (FWHM), for an average power of 20 MW. The burn pattern, shown in Figure 20, indicates an extracted area of 5.6  $\text{cm}^2$ . Since the output coupler was an 80% reflector, the intracavity intensity must have been 18  $\text{MW}/\text{cm}^2$  or about eight times the saturation intensity. The specific energy extracted from a volume of 112  $\text{cm}^3$  was 29 J/l.

Under the same conditions as above, the e-beam alone gave 1.9 J laser output for a specific energy of 17 J/l. The stopping power of the laser gas was 7.4 kV/cm/atm (including a factor of 3 to account for the effects of electron scattering) which gives a deposited energy of

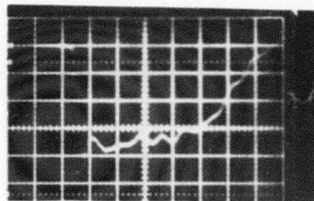
$$\begin{aligned} \mathcal{E}_{\text{eb}} &= 7.4 \text{ kV/cm/atm} \cdot 3 \text{ atm} \cdot 40 \text{ A/cm}^2 \cdot 220 \text{ ns} \\ &= 195 \text{ J/l} \end{aligned}$$

Thus the laser efficiency with pure e-beam pumping was

$$\eta_{\text{eb}} = 17 \text{ J/l} / 195 \text{ J/l} = 9\%$$

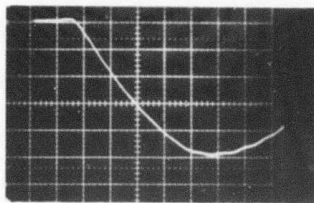


SUSTAINER  
VOLTAGE



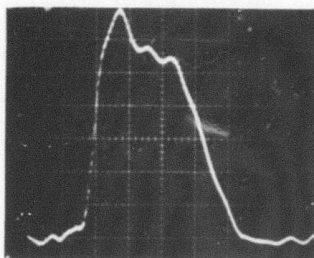
1.25 kV/Div

SUSTAINER  
CURRENT



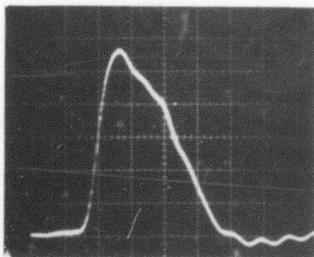
4 kA/Div

LASER  
POWER



3.2 J

LASER  
POWER  
(E-BEAM  
ONLY)



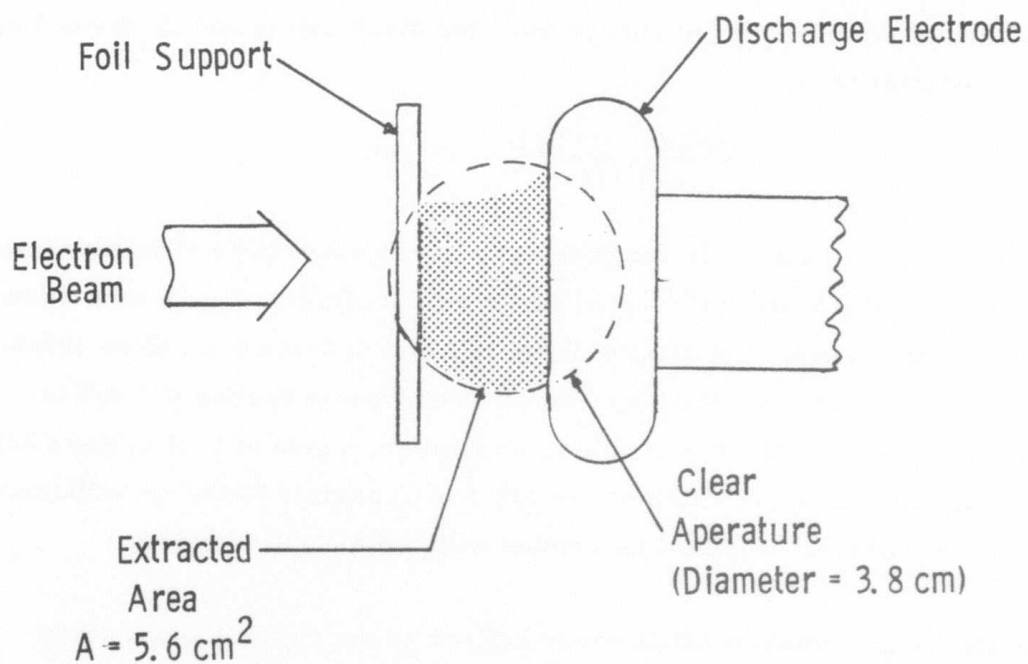
1.9 J

50 nsec/Div

Figure 19. Highest Energy Regime



BURN PATTERN



$$\text{Volume} = 20 \text{ cm} \times 5.6 \text{ cm}^2 = 112 \text{ cm}^3$$

Figure 20. Extracted Volume from NRTC 0.1 Liter Device

The discharge power density can be found by integrating under the current-voltage waveforms of Figure 19 up to the termination of the laser pulse.

This gives

$$\begin{aligned}\epsilon_d &= \frac{2}{\pi} \cdot 2.25 \text{ kV/cm} \cdot 250 \text{ A/cm}^2 \cdot 220 \text{ ns} \\ &= 79 \text{ J/l}\end{aligned}$$

The laser efficiency for the combined e-beam puls discharge pumping was therefore,

$$\eta = \frac{29 \text{ J/l}}{195 \text{ J/l} + 79 \text{ J/l}} = 11\%$$

The efficiency for converting discharge power into laser output can be defined as the increase in extracted energy when the discharge is added, divided by the added energy, i. e.

$$\eta_d = \frac{29 \text{ J/l} - 17 \text{ J/l}}{79 \text{ J/l}} = 15\%$$

The discharge efficiency is composed of a power conversion efficiency from electrical power to the  $\text{KrF}^*$  upper laser level multiplied by the extraction or cavity efficiency. The first of these is found in Section 4.1 to be 36% for the present conditions, while the second is derived in Section 4.3 and is given in Equation (14). For a ratio of absorption to gain of 0.12 (Figure 32), the optimum extraction efficiency is 43% for an overall discharge efficiency of 15%, which is in excellent agreement with the measured value.

The discharge enhancement factor is defined as the ratio of total energy deposited (e-beam + discharge) to the energy deposited by the e-beam. In the present case, this factor was 1.4. In light of the greater laser efficiency with discharge pumping, an effort was made to increase this value by reducing the e-beam current density and increasing the pulselength. The results are shown in Figure 21.

MARX  
CURRENT

220 J Stored

SUSTAINER  
VOLTAGE

600 V/Div

SUSTAINER  
CURRENT

4 kA/Div

LASER  
POWER

420 mJ

LASER  
POWER  
(E-BEAM ONLY)

180 mJ

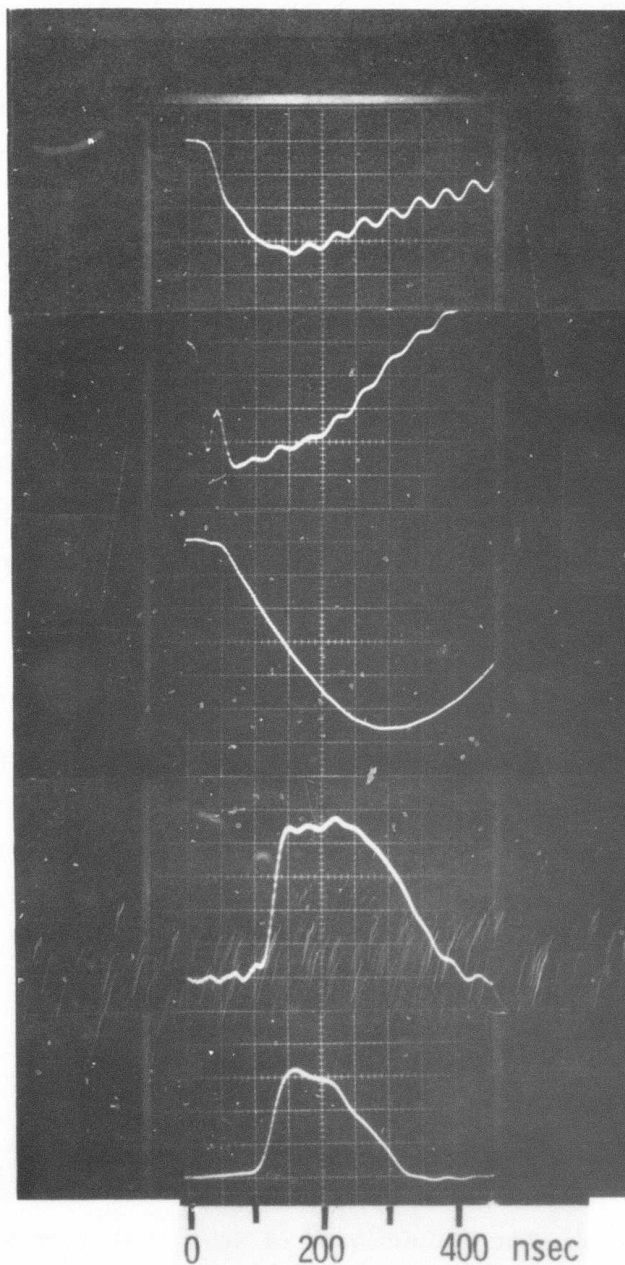


Figure 21. Long Pulse Regime



### 3.3 Additional Discharge Laser Candidates

Northrop has studied a variety of e-beam pumped rare gas halide and transfer lasers, which are discussed in this section. These molecules appear to be good candidates for e-beam controlled discharge pumping and can be used in the same laser device as KrF. The most promising candidates appear to be the xenon halide lasers and the Ar-I<sub>2</sub> transfer laser. A review of these candidates is presented in this section.

#### 3.3.1 Xenon Halide Lasers

Recently, Velazco and Setser<sup>9</sup> predicted that the xenon halides might be good laser candidates in the near uv spectral region. Northrop verified the prediction in the development of e-beam pumped XeF,<sup>1</sup> XeCl,<sup>5</sup> and XeBr<sup>5</sup> lasers. Figure 22 shows the measured spectra of several rare gas halide lasers.

The experimental arrangement for the xenon halide studies was similar to that described for KrF in Section 3.1. High power laser emission was observed from xenon fluoride at 351.1 and 353.1 nm. A peak laser power of 0.5 MW was obtained by using a mixture of Ar, Xe, and NF<sub>3</sub> in the ratio of 250:25:1 at a total pressure of 1.7 atm. Using a coaxial electron gun, 80 mJ was obtained in a 100 ns pulse. An oscillogram of the laser pulse is shown in Figure 23.

The high pressure emission spectrum, shown in Figure 22, is similar to those reported by Velazco and Setser<sup>9</sup> for XeF\* at low pressures, except that diffuse continuum on the long wavelength side is completely missing at higher pressures. The 350 nm band of XeF\* is thought to be due<sup>9</sup> to transitions from a coulombic upper  $2\Sigma^+$  state to a weakly bound  $2\Sigma^+$  ground state. Strong XeF emission appears as two intense sharp bands at 351.1 nm and 353.1 nm, each about 0.25 nm wide and nearly equal in intensity. It

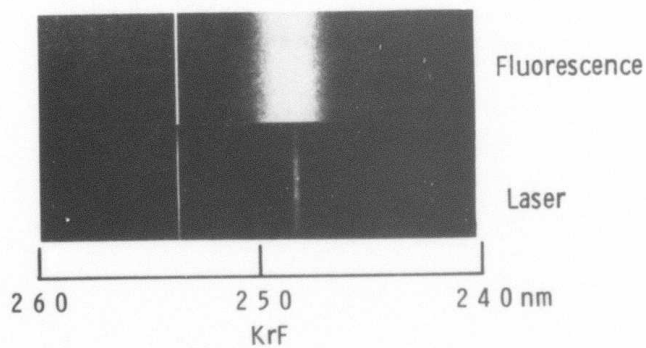
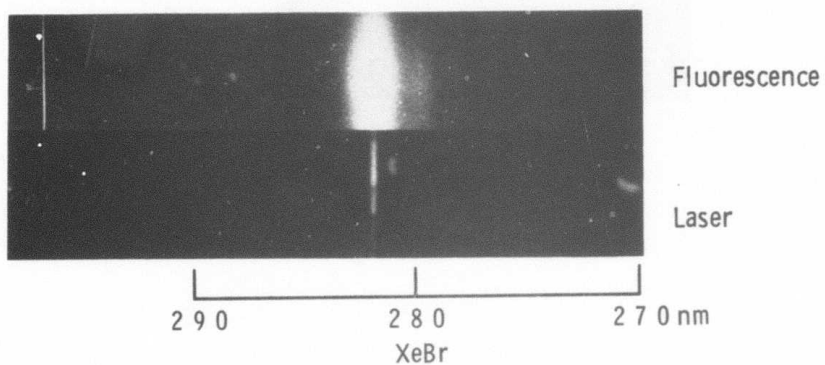
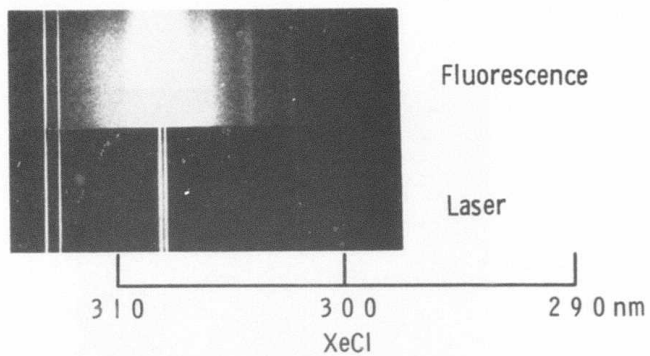
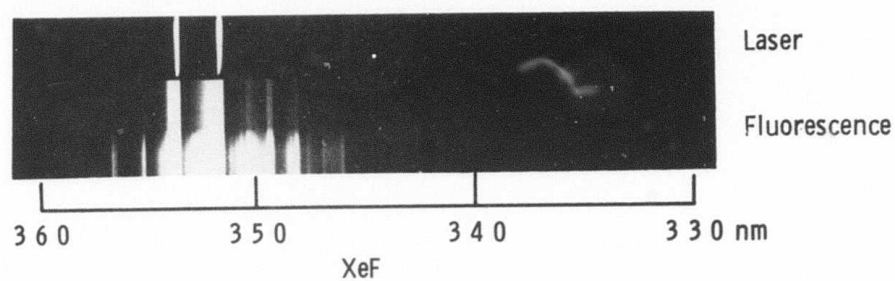


Figure 22. Fluorescence and Laser Spectra for XeF, XeCl, XeBr, and KrF.

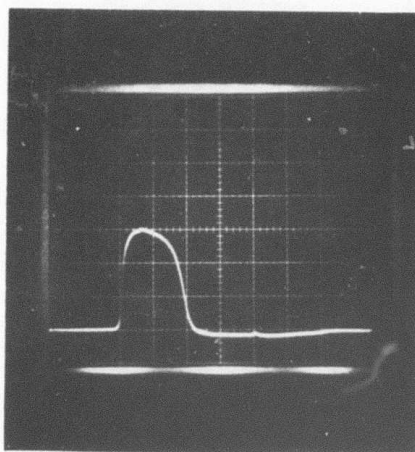


Figure 23. Coaxially pumped laser pulse from  
1 atm mixture of Ar, Xe and  $\text{NF}_3$   
(250:25:1); vertical axis: 300 kW/div,  
horizontal axis: 50 nsec/div.

appears that XeF does not accumulate since no drastic reduction in intensity was observed in successive shots. This is probably due to the reaction of ground state XeF with NF<sub>2</sub> to reform NF<sub>3</sub> and Xe. Such chemical removal may prevent "bottlenecking" and improve long pulse laser operation.

Production of XeF\* in a direct reaction of the xenon metastable atom Xe\* (<sup>3</sup>P<sub>2</sub>) with a halogen containing molecule is well known,<sup>9</sup> since it is very similar to the reaction of an alkali metal atom with a halogen forming an alkali halide. Relevant reactions are shown in Table III. In e-beam excited Xe gas, Xe\* metastables are formed via Xe<sup>+</sup>, since the primary mechanism of energy deposition by the high energy (H.E.) electrons of the e-beam is by ion-electron pair production. Ar<sup>+</sup> created by high energy electrons is quickly converted to Ar\* by Reactions 2 and 3. At the above pressures, formation of Xe\* from Ar\* by Reaction 6 is favored in contrast to the formation of either Ar<sub>2</sub>\* or ArF\* by Reactions 4 and 5, respectively. Even if the rate of Reaction 5 was somewhat higher than estimated, the rate of formation of ArF\* would still be low since the number density of Xe is an order of magnitude higher than that of NF<sub>3</sub>. The 10% concentration of Xe also directly absorbs an additional 30% energy since its stopping power is nearly three times higher than Ar. Additional Xe<sup>+</sup> produced in this way is also converted into Xe\* by a mechanism similar to that of Ar.

Conversion of Xe\* into XeF\* by Reaction 8 clearly predominates at these pressures compared to excimer formation given by Reaction 7. Severe quenching of XeF\*, presumably by either NF<sub>3</sub>, NF<sub>2</sub> (Reaction 9), or Xe is the most important loss mechanism, which must be prevented to obtain an efficient laser operation. Such behavior appears<sup>13</sup> to be generally true for most halogen containing molecules. This suggests that the mole fraction of NF<sub>3</sub> should be as small as possible. On the other hand, a favorable rate of formation of XeF\* and the gain necessary for laser operation require a certain minimum concentration of NF<sub>3</sub>.



Table III. Important Processes for the XeF Laser

REACTION	RATES
1 $\text{Ar} + \text{H.E.e}^- \rightarrow \text{Ar}^+ + \text{e}^- + \text{Ar}^* + \text{H.E.e}^-$	
2 $\text{Ar}^+ + 2 \text{Ar} \rightarrow \text{Ar}_2^+ + \text{Ar}$	$2.5 \times 10^{-31} \text{ cm}^6/\text{sec}$
3 $\text{Ar}_2^+ + \text{e}^- \rightarrow \text{Ar}^* + \text{Ar}$	$7 \times 10^{-7} \text{ cm}^3/\text{sec}$
4 $\text{Ar}^* + 2 \text{Ar} \rightarrow \text{Ar}_2^* + \text{Ar}$	$1.14 \times 10^{-32} \text{ cm}^6/\text{sec}$
5 $\text{Ar}^* + \text{NF}_3 \rightarrow \text{ArF}^* + \text{NF}_2$	$\sim 10^{-10} \text{ cm}^3/\text{sec}$
6 $\text{Ar}^* + \text{Xe} \rightarrow \text{Ar} + \text{Xe}^*$	$2 \times 10^{-10} \text{ cm}^3/\text{sec}$
7 $\text{Xe}^* + \text{Xe} + \text{Ar} \rightarrow \text{Xe}_2^* + \text{Ar}$	$\sim 10^{-32} \text{ cm}^6/\text{sec}$
8 $\text{Xe}^* + \text{NF}_3 \rightarrow \text{XeF}^* + \text{NF}_2$	$\sim 10^{-9} \text{ cm}^3/\text{sec}$
9 $\text{XeF}^* + \text{NF}_3 (\text{NF}_2) \rightarrow \text{Xe} + \text{F} + \text{NF}_3 (\text{NF}_2)$	$\sim 10^{-9} \text{ cm}^3/\text{sec}$
10 $\text{XeF}^* \rightarrow \text{Xe} + \text{F} + h\nu$	$\sim 8 \times 10^6/\text{sec}$

Similar results were obtained for XeCl and XeBr. A summary of xenon halide laser output is found in Table IV. These molecules should make good discharge pumped laser candidates.

### 3.3.2 Ar-I<sub>2</sub> Transfer Laser

E-beam pumping of noble gases at high pressures has been very useful for the efficient production of electronically excited rare gas metastables. These species may subsequently serve as a pump for some appropriate acceptor laser molecule. This concept was demonstrated at Northrop<sup>14</sup> by the operation of an Ar-N<sub>2</sub> transfer laser. However, efficiencies greater than 3% have not been possible due to an unfavorable branching ratio to the upper laser state of the N<sub>2</sub> second positive transition.

Tellinghuisen<sup>15</sup> has suggested that I<sub>2</sub> could be utilized as a tunable uv laser. McCusker<sup>16</sup> has shown that the fluorescence yield of e-beam produced Ar<sup>\*</sup> transfer to I<sub>2</sub> is 70%. Subsequent experiments at Northrop<sup>6</sup> demonstrated Ar-I<sub>2</sub> transfer laser operation at 342 nm. The laser developed a peak output power of 3.6 MW in a 10 ns pulse. Experiments were performed at room temperature. Since a heated gas cell is necessary to obtain sufficient concentrations of I<sub>2</sub> vapor from solid iodine, excited I<sub>2</sub> molecules were obtained from an e-beam pumped mixture of Ar and CF<sub>3</sub>I (250:1) at 10 atm. I<sub>2</sub> fluorescence spectra at 342 nm obtained from this mixture was identical to that of Ar and I<sub>2</sub> (3800:1) at 1 atm.

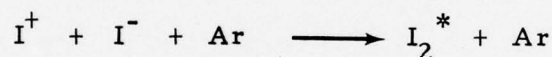
The experimental arrangement was similar to that used with KrF, discussed earlier in Section 3.1. A Physics International Pulserad 110A electron gun provided the 2 x 10 cm, 1 MeV, 20 kA, 20 ns electron beam. The resonator was formed by a total reflector with an 85% reflecting output coupler containing an extraction volume of 30 cm<sup>3</sup>.

Table IV.

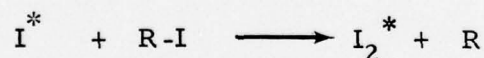
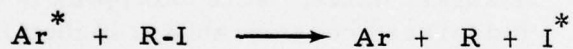
XeF	Ar:Xe:NF <sub>3</sub> 500 kW, 10 ns 351.1 and 353.1 nm	250:25:1	1.7 atm
XeCl	Ar:Xe:Cl <sub>2</sub> 18 kW, 10 ns 308 nm	560:62:1	3.4 atm
XeBr	Ar:Xe:CF <sub>3</sub> Br 45 kW, 10 ns 282 nm	700:75:1	2 atm

Laser and fluorescence output intensities were measured with an ITT FW 114A photodiode in conjunction with a Tektronix 7904 oscilloscope. An oscillogram of the laser pulse is shown in Figure 24. Laser output energy was measured by a Gen Tec model ED 200 integrating pyroelectric detector. A SPEX 1800 1 m Czerny-Turner spectrograph was used for spectral measurements. The fluorescence spectrum of  $I_2$  is shown in Figure 25(a). The laser spectrum is shown in Figure 25(b). Assignments of these lines are given in Table V.

Several Ar- $I_2$  transfer mechanisms<sup>6,7</sup> have been proposed to explain the formation of  $I_2$  in the observed time delay between initiation of excitation and laser onset. Most proposed mechanisms depend on  $I^-$  as the majority negative charge carrier with subsequent Thompson three-body recombination to form  $I_2^*$ :



It is not very probable that  $I^-$  is the majority negative carrier. A more plausible mechanism for  $I_2^*$  production uses  $Ar^*$  as the precursor and is shown below:



where R is an organic radical such as  $CF_3$  or H. The partial pressures of  $Ar^*$  and  $CF_3I$  will allow a sufficient number of collisions to form  $I_2^*$  within the 20 ns delay as shown in Figure 24.

The Ar- $I_2$  transfer laser is very promising for discharge pumping. Iodine donors, such as HI or  $CF_3I$ , have lower electron attachment than  $F_2$ . They are also much less corrosive. In preliminary discharge studies of Ar- $I_2$ , 63 mJ was obtained in a 150 ns pulse at 342 nm using a mixture



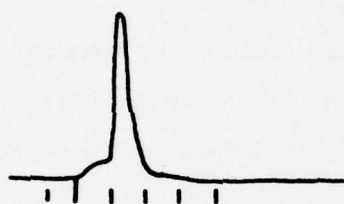


Figure 24. Laser pulse from a mixture of 11 Torr  $\text{CF}_3\text{I}$  and 4 atm Ar with total reflectors ( $\sim 99\%$ ). The time scale is 20 nsec/div. Note the delay between the initiation of excitation (indicated by the wide line) and laser onset. This delay was observed to decrease considerably at higher Ar pressure.

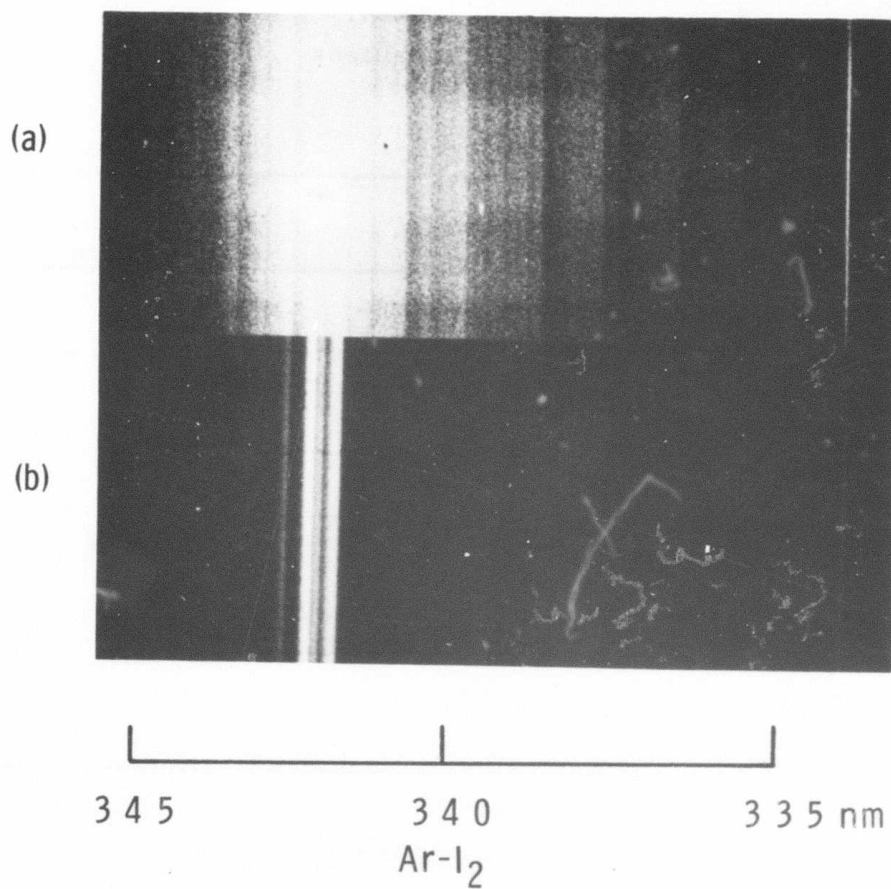


Figure 25. (a) Fluorescence spectrum of Ar + CF<sub>3</sub>I which is similar to that of Ar + I<sub>2</sub>.  
 (b) Laser spectrum of Ar + CF<sub>3</sub>I. The output was highly attenuated to avoid film saturation.

Table V.  $I_2$  Transitions

Fluorescence <sup>a</sup> $\lambda(\text{nm})$	$v'-v''$	Laser $\lambda(\text{nm})$
341.861	0-12	} 342.0 $\pm$ 0.1
341.920	2-15	
342.199	3-17	342.3
342.335	1-14	342.4
342.682	2-16	} 342.8
342.723	0-13	

a. Tellinghuisen (private communication).

of Ar and HI (310:1) at a total pressure of 4 atm. The advantages of Ar-I<sub>2</sub> are summarized in Table VI.

Table VI. Advantages of the Ar-I<sub>2</sub> Transfer Laser

- High Quantum Efficiency  
~ 30% for Discharge Pumping
- Favorable Atmospheric Transmission  
Characteristics at 342 nm
- Low Electron Attachment
- Ease of Gas Handling



#### 4.0 ANALYTICAL MODELING

##### 4.1 Electron Kinetics in the KrF Laser

Since discharge pumping of  $\text{KrF}^*$  has been demonstrated<sup>17</sup> to be more efficient than e-beam pumping, it is desirable to load as much energy into the discharge as possible. An analysis of the limit of energy loading and the laser efficiency requires an understanding of the electron and excited-state kinetics in the discharge. If the ratio of metastable density to ground state neutral density,  $m/N$ , is  $10^{-5}$  or less, then electron-metastable collisions have a negligible effect on the electron energy distribution<sup>18</sup> and the electron kinetics can be decoupled from the excited-state chemistry model. This allows a parameter study to be made of electron transport and excitation processes in the KrF laser which can be used as input to a complete laser model including optical resonator and external circuit.<sup>19</sup>

The following discussion will emphasize the importance of including collisions between electrons via a screened Coulomb potential in the Boltzmann analysis of the heavy rare gases. At fractional electron densities typical of e-beam sustained KrF laser discharges ( $n/N = 3 \times 10^{-6} - 3 \times 10^{-5}$ ) these collisions appreciably alter both the electron mobility and the rate constants for excitation and ionization. Because of the sensitivity of the high energy tail of the electron energy distribution (Figure 26), the effect of electron-electron collisions is most significant for those processes with the highest threshold energies. The reason electron-electron collisions are not important in modeling the CO and  $\text{CO}_2$  lasers is that the pumping occurs at much lower energies and typical values of  $n/N$  are only  $10^{-7}$ . These collisions must be considered, however, in analyzing discharge stability, because of the large effect on ionization rates.

The method employed in this study to solve the Boltzmann transport equation has been described previously.<sup>20</sup> The contribution to the collision

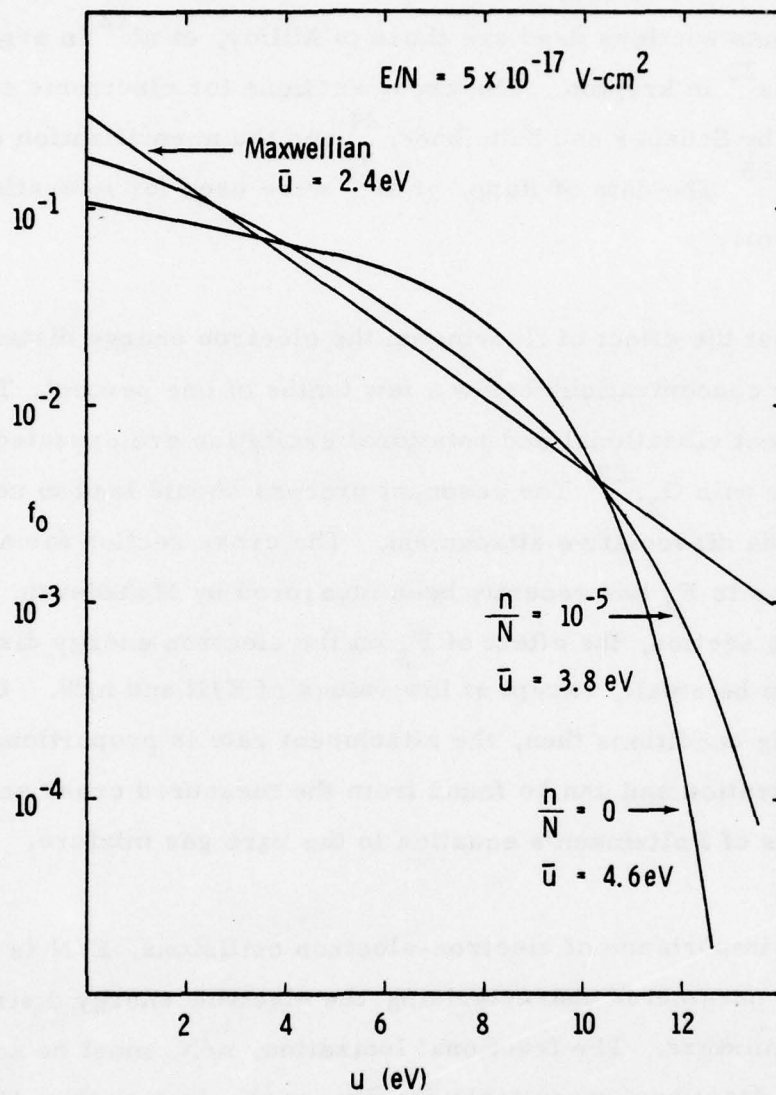


Figure 26. Electron Energy Distribution in Ar-Kr

term arising from Coulomb collisions between electrons is derived by Shkarofsky, et al.<sup>21</sup> The value of  $\ln \Lambda$  is taken to be 10, where  $\Lambda$  is the ratio of Debye length to the impact parameter for a 90° deflection. The momentum transfer cross sections used are those of Milloy, et al.<sup>22</sup> in argon and Frost and Phelps<sup>23</sup> in krypton. The cross sections for electronic excitation were measured by Schaper and Scheibner,<sup>24</sup> and the normalization checked by Jacob, et al.<sup>25</sup> The data of Rapp, et al.<sup>26</sup> were used for ionization of ground state atoms.

It is assumed that the effect of fluorine on the electron energy distribution is negligible for concentrations below a few tenths of one percent. The cross sections for direct vibrational and rotational excitation are expected to be small in analogy with  $O_2$ .<sup>27</sup> The resonant process should lead to negative ion production via dissociative attachment. The cross section for attachment of electrons to  $F_2$  has recently been measured by Mahadevan, et al.<sup>28</sup> Using this cross section, the effect of  $F_2$  on the electron energy distribution was found to be small, except at low values of  $E/N$  and  $n/N$ . Under normal operating conditions then, the attachment rate is proportional to the fluorine concentration and can be found from the measured cross section and the solutions of Boltzmann's equation in the rare gas mixture.

Because of the importance of electron-electron collisions,  $E/N$  is no longer the sole parameter characterizing the electron energy distribution in a given gas mixture. The fractional ionization,  $n/N$ , must be specified as well. If the fractional metastable density,  $m/N$ , is less than  $10^{-5}$ , it is not an important parameter. Since the largest fractional metastable density consistent with stable discharge operation is about  $3 \times 10^{-5}$ , the effects of superelastic collisions and metastable ionization on the electron energy distribution can be neglected. In a stable discharge, therefore, we can completely characterize the electron properties in a given gas mixture with the two parameters,  $E/N$  and  $n/N$ .



The electron drift velocity and mean energy are plotted in Figure 27 as a function of  $E/N$  for typical values of  $n/N$  in a 95% Ar 5% Kr mixture. The curves labeled  $n/N = 0$  apply to fractional ionizations below about  $10^{-7}$ . The drift velocity is found to be more than a factor of two higher at typical electron densities than it is at low electron density where electron-electron collisions are unimportant. The calculated drift velocity in pure argon with  $n/N = 0$  agrees within 5% with the experimental data of Pack, et al,<sup>29</sup> Robertson,<sup>30</sup> and Brambring<sup>31</sup> over the  $E/N$  range from  $10^{-19}$  Vcm<sup>2</sup> to  $10^{-15}$  Vcm<sup>2</sup>. The power loading into the discharge is given by  $E \cdot J = eN^2 \frac{n}{N} v_e \left( \frac{E}{N} + \frac{n}{N} \right) \frac{E}{N}$ . As a result of the  $n/N$  dependence of  $v_e$ , this function will increase faster than linearly with  $n/N$  at constant  $E/N$ .

All the energy which goes into the discharge is converted through various channels into heat, electronic excitation or ionization of the gas. The dominant processes include heating by momentum transfer in elastic collisions and excitation of various electronic states in argon and krypton. The cross sections for excitation of these electronic states are lumped together for each gas and represent an effective cross section for production of the metastable. The fractional power into each of these channels is plotted in Figure 28 as a function of  $E/N$  for typical values of  $n/N$ . The power going into ionization of metastables and ground state atoms is negligible in the parameter range considered here. The effect of electron-electron collisions is dramatic in moving the range of efficient production of metastables to lower values of  $E/N$ . This has a significant impact on the predicted operating regime of the KrF laser.

The highest specific laser energy to date from an e-beam sustained discharge in Ar-Kr-F<sub>2</sub> was observed at an  $E/N = 3 \times 10^{-17}$  Vcm<sup>2</sup>.<sup>17</sup> The measured discharge efficiency was 20%, and yet without electron-electron collisions the theory would predict virtually no pumping of metastable states by the discharge at this  $E/N$ .



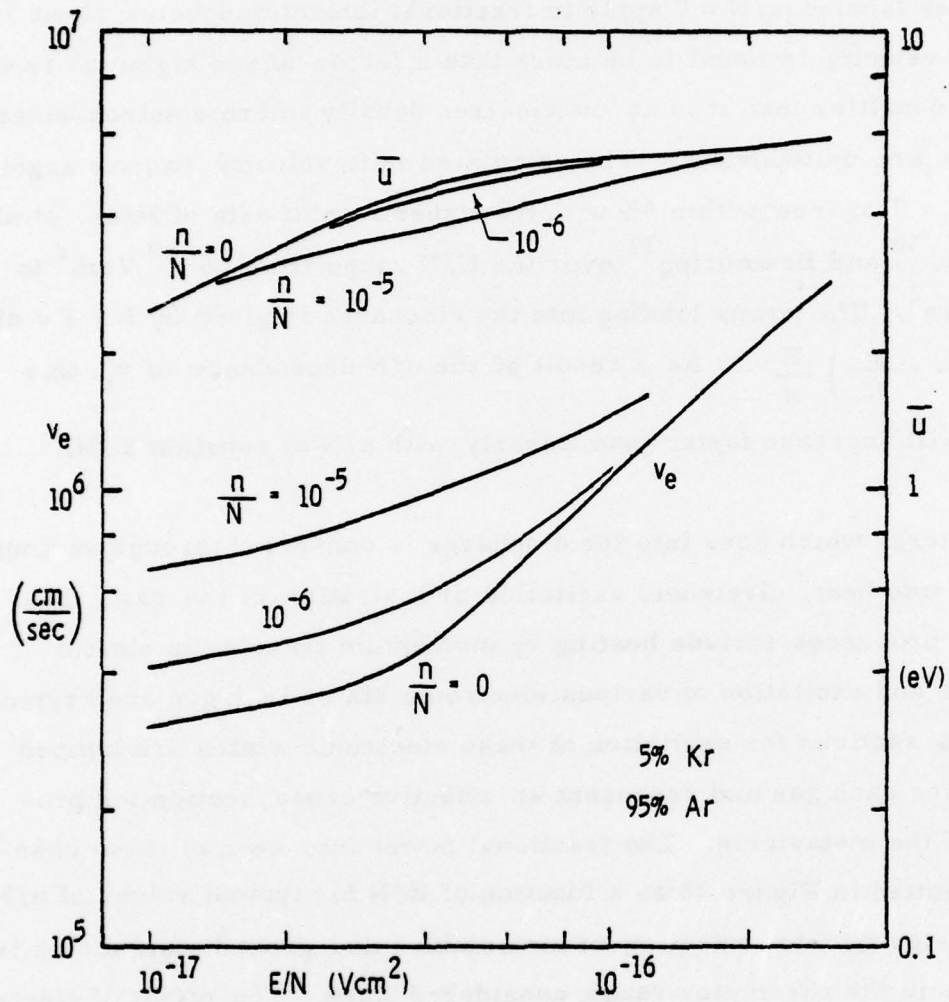


Figure 27. Electron Drift Velocity and Mean Energy

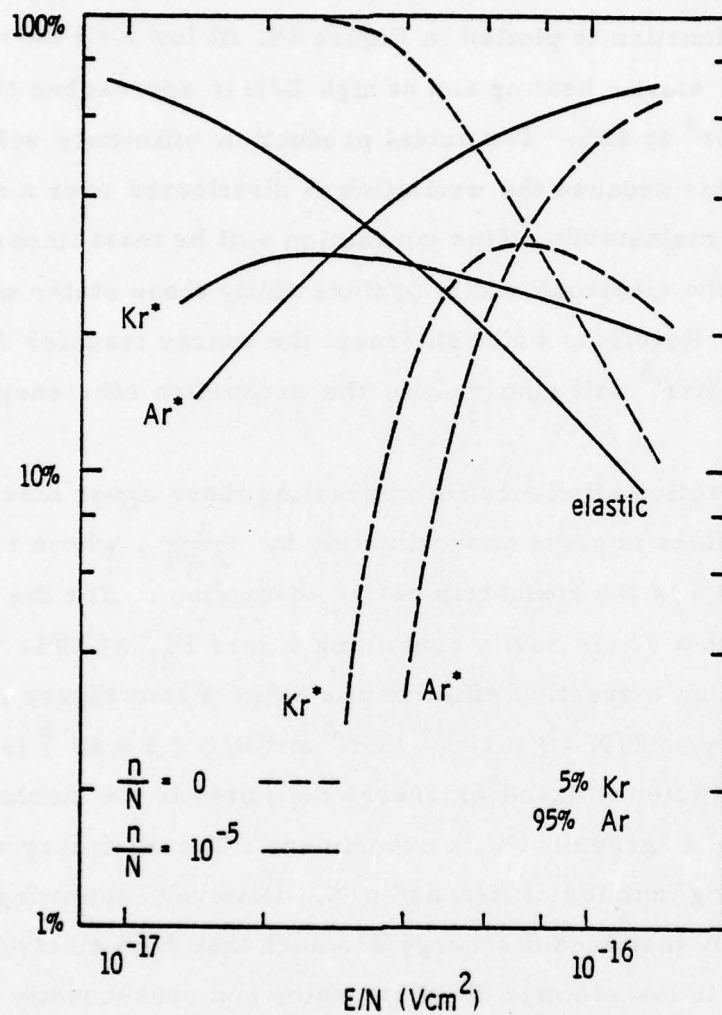


Figure 28. Discharge Power Partitioning

The quantum efficiency for producing  $\text{KrF}^*$  can be derived from the power partitioning curves by defining  $\eta = \frac{h\nu}{e} [f(\text{Ar}^*) / 11.8 \text{ eV} + f(\text{Kr}^*) / 9.9 \text{ eV}]$ . The numerator in each term is the fraction of discharge power going into the metastable and the denominator is the energy of the metastable. This function is plotted in Figure 29. At low  $E/N$  the efficiency falls off because of elastic heating and at high  $E/N$  it approaches the quantum efficiency of  $\text{Ar}^*$  at 42%. The actual production efficiency will be slightly less than this because the excitation is distributed over a number of levels above the metastable. This correction will be least important at low  $E/N$  where the electrons excite preferentially those states with the lowest thresholds. Reactions which intercept the energy transfer from the metastables to  $\text{KrF}^*$  will also reduce the production efficiency.

The maximum extraction efficiency for converting these upper laser levels to laser photons is given approximately by  $\frac{t}{a + t}$ , where  $t$  is output coupling and  $a$  is the round trip cavity absorption. For the device in Reference 17 with a 50 cm cavity containing 4 torr  $\text{F}_2$ ,  $a \approx 20\%$ . With  $t = 20\%$ , the maximum extraction efficiency is 50%. From Figure 29 the discharge efficiency at  $E/N = 3 \times 10^{-17} \text{ Vcm}^2$  and  $n/N = 3 \times 10^{-5}$  is 36%. The resulting net efficiency based on energy deposited in the discharge is therefore 18% in good agreement with experiment. The efficiency would appear to be a strong function of  $E/N$  and  $n/N$ . However, operating conditions in an e-beam sustained discharge are such that high electron densities give rise to low electric field strengths and consequently the discharge efficiency is nearly constant.

In conclusion, we have presented a parametric study of the electron kinetics in an Ar-Kr- $\text{F}_2$  discharge. It was found that  $E/N$  and  $n/N$  are the critical parameters, while  $m/N$  and  $[\text{F}_2]/N$  can be neglected when they are smaller than  $10^{-5}$  and  $10^{-3}$  respectively. Electron-electron collisions play a significant role in increasing electron mobility and in raising the metastable

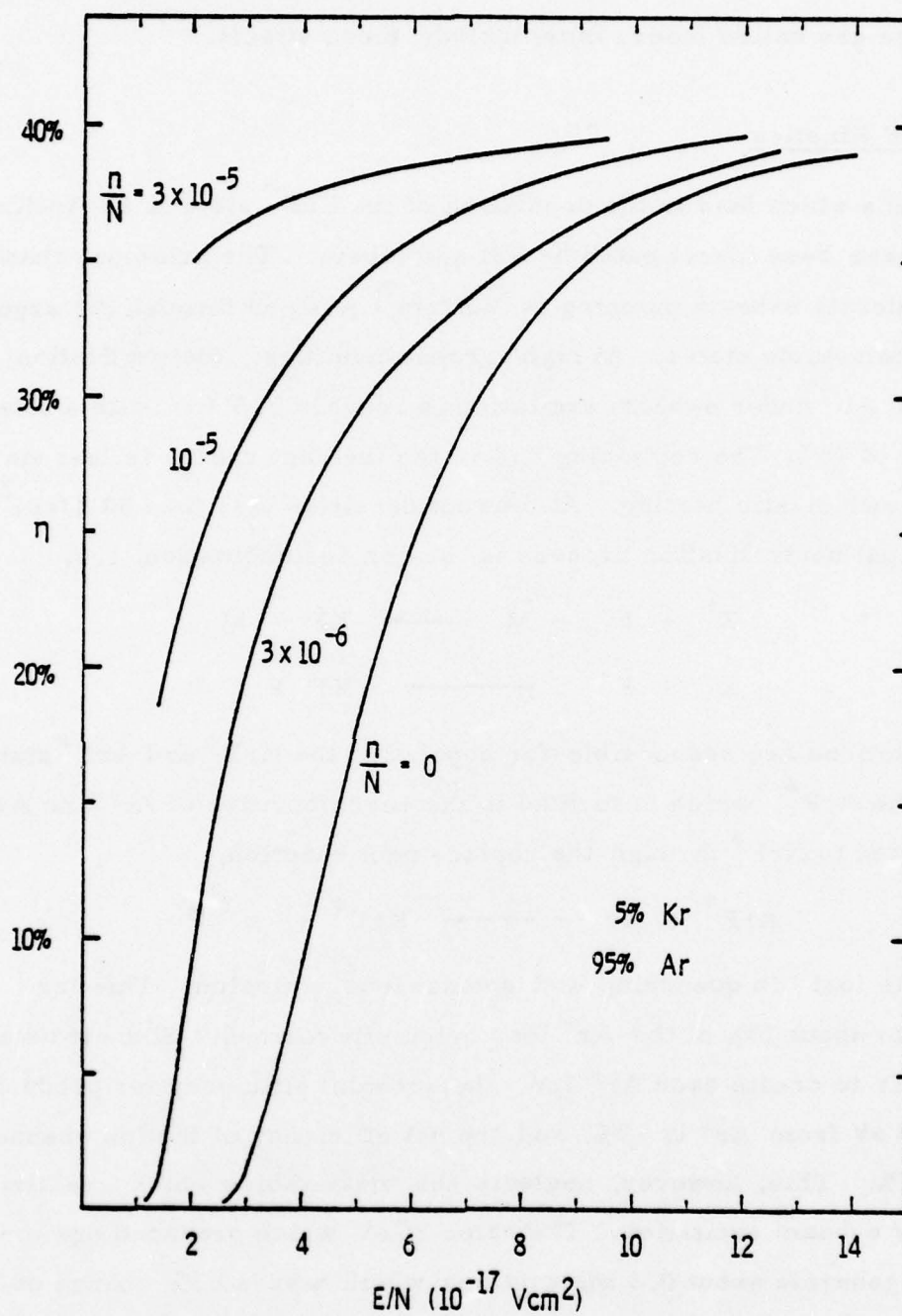


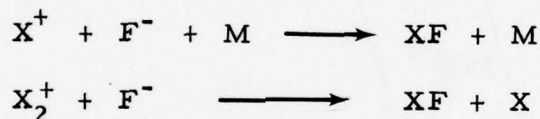
Figure 29. Quantum Efficiency for Producing  $\text{KrF}^*$



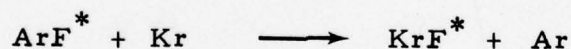
production efficiency at low values of  $E/N$ . Any comprehensive model of the rare gas halide lasers must include these effects.

#### 4.2 KrF Kinetics

The kinetics which lead to the population of the  $\text{KrF}^*$  state in an Ar-Kr- $\text{F}_2$  mixture have been investigated by SRI and others. The principal channels under moderate e-beam pumping ( $< 50 \text{ A/cm}^2$ ) proceed through the argon ion and metastable states. At high current densities, the production of  $\text{Ar}^+$  and  $\text{Ar}^*$  under e-beam excitation is roughly 3.5 to 1 with a total efficiency of 75%. The remaining 25% of the incident energy is lost via radiation and elastic heating. At current densities less than  $50 \text{ A/cm}^2$  the principal neutralization process is ion-ion recombination, i. e.



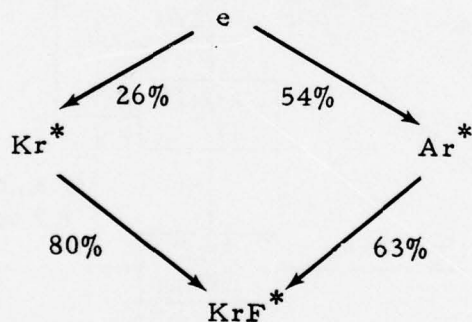
These reactions are responsible for populating the  $\text{KrF}^*$  and  $\text{ArF}^*$  states. Some of the  $\text{ArF}^*$ , which is formed in the recombination of  $\text{Ar}^+$  and  $\text{Ar}_2^+$ , is converted to  $\text{KrF}^*$  through the replacement reaction,



The rest is lost via quenching and spontaneous emission. This loss amounts to about 10% of the  $\text{Ar}^+$  ions originally formed. Since it takes about 26 eV to create each  $\text{Ar}^+$  ion, the quantum efficiency for producing  $\text{KrF}^*$  at 5 eV from  $\text{Ar}^+$  is 19%, and the net efficiency of the ion channel is then 17%. This, however, neglects the metastables which are also formed by e-beam excitation. The same 26 eV which produced one ion will also generate about 0.3 metastables which have a 63% chance of forming  $\text{KrF}^*$ . This raises the overall efficiency for e-beam pumping to 20%. The neutral channel processes will be discussed below.

Under discharge pumping of KrF, about 80% of the input power goes into excited rare gas states  $\text{Ar}^*$  and  $\text{Kr}^*$ . The remaining 20% is lost in elastic scattering

and dissociative attachment to  $F_2$ . The ratio of  $Ar^*$  to  $Kr^*$  produced is about two to one, Figure 28. Very few ions are generated by the discharge. There are two dominant channels for converting  $Ar^*$  to  $KrF^*$ , Figure 30 one through the  $ArF^*$  state and the other through the  $Kr^*$  state. With a total pressure of three atmospheres and 0.17%  $F_2$ , about 60% of the  $Ar^*$  react with  $F_2$  to form  $ArF^*$ , which has a 55% chance of being converted to  $KrF^*$ . (At two atmospheres with the same percentage of  $F_2$ , about 65% of the  $Ar^*$  go through this channel.) About 37% of the  $Ar^*$  undergo excitation transfer to  $Kr^*$ , either directly or via  $Ar_2^*$ . The remaining 3% end up as  $Ar_2F^*$ . The  $Kr^*$ , formed either through this channel or directly by the discharge, have a 60% chance of producing  $KrF^*$ . The other 40% go into forming the rare gas dimers  $ArKr^*$  and  $Kr_2^*$ . It is believed that when these excited states react with  $F_2$  about half of them produce  $KrF^*$  and the rest form the  $ArKrF^*$  and  $Kr_2F^*$  states. The resulting discharge efficiency is summarized below.



Quantum Efficiency	<u>51%</u>	<u>42%</u>
Net	10.6%	14.3%
Sum	25%	

The discharge pumping of  $KrF^*$  is slightly more efficient than pure e-beam pumping based on energy deposited. However, wall-plug efficiency for the e-beam device will be much less due to a 25% loss in the foil and foil supports and up to 75% transmission through the plenum. The e-beam

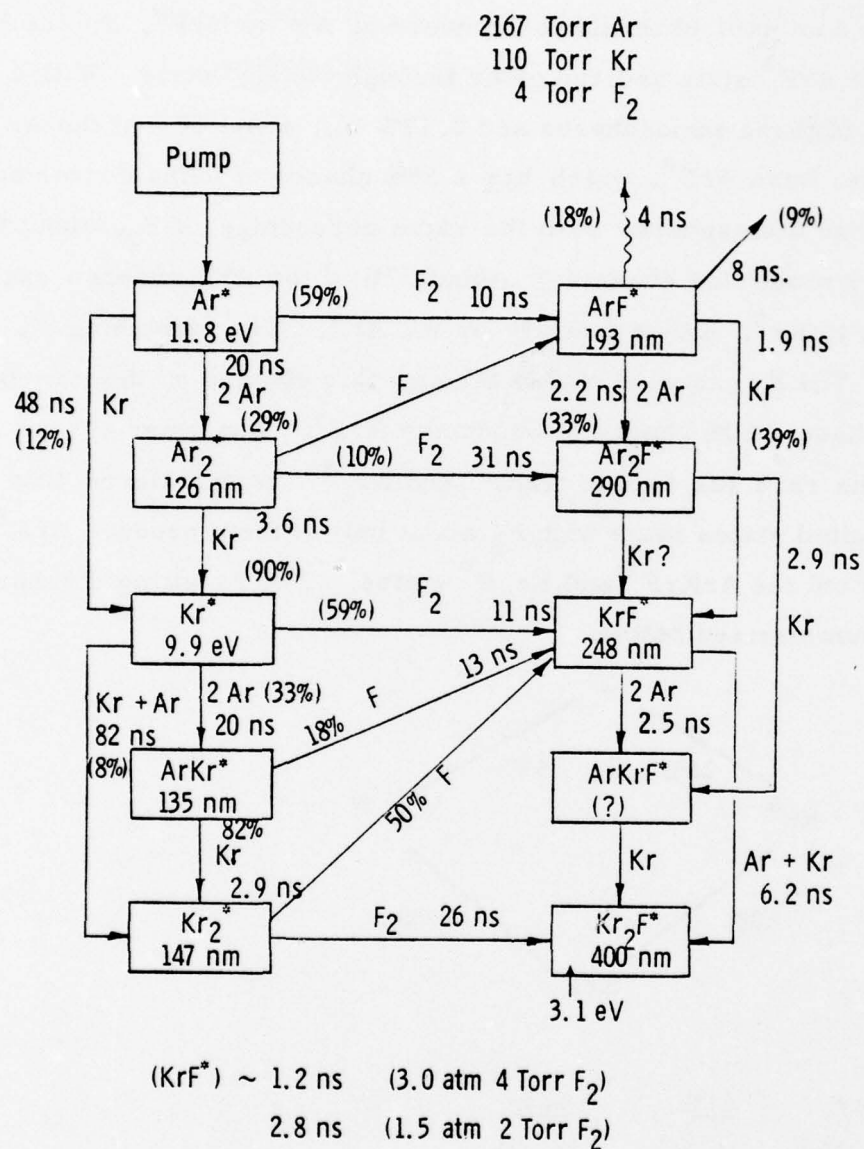


Figure 30. Neutral Channels

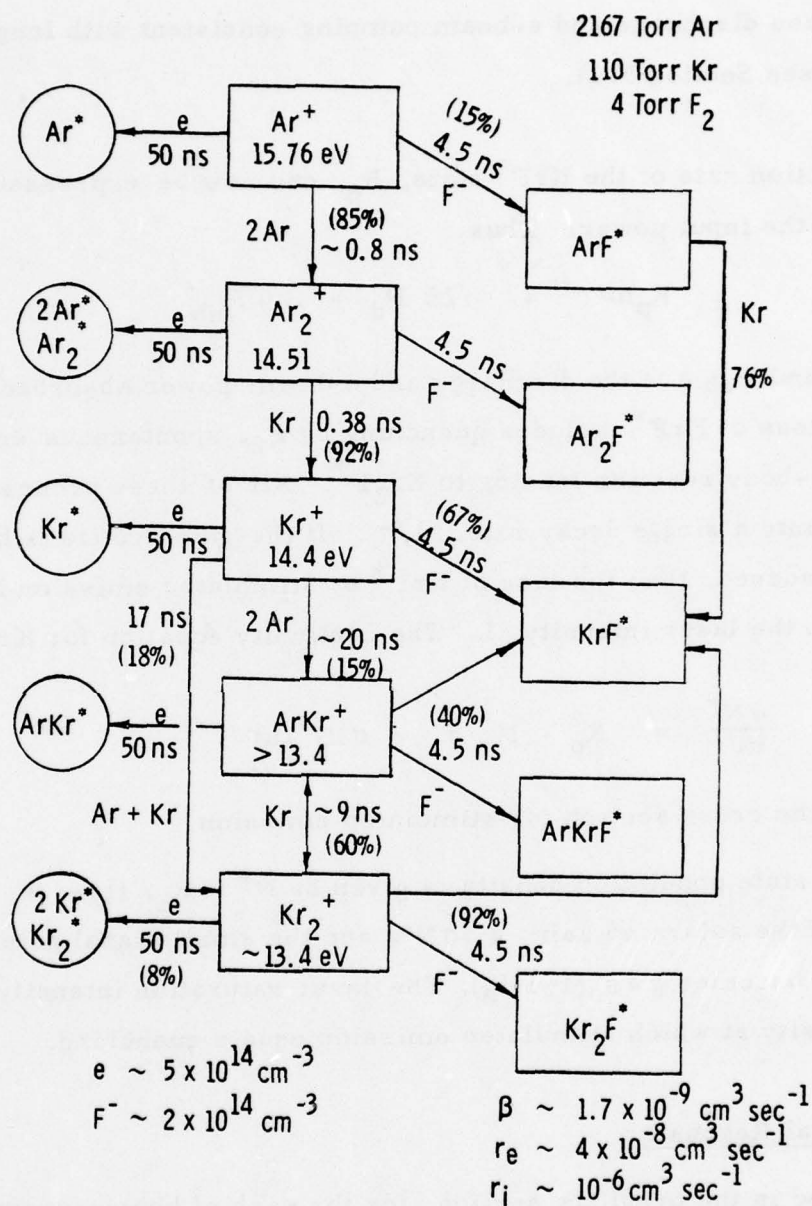


Figure 31. Ion Channels



also produces molecular ions which absorb at the laser frequency. In a practical device it is therefore desirable to achieve the highest possible ratio between discharge and e-beam pumping consistent with long pulse stability (see Section 5.1).

The production rate of the  $\text{KrF}^*$  state,  $R_p$ , can now be expressed as a function of the input power. Thus,

$$R_p h\nu = .25 P_d + .20 P_{eb} \quad (1)$$

where  $P_d$  and  $P_{eb}$  are the discharge and e-beam power absorbed by the gas. The loss of  $\text{KrF}^*$  includes quenching by  $\text{F}_2$ , spontaneous emission and a three-body reaction leading to  $\text{Kr}_2\text{F}^*$ . All of these processes will be lumped into a single decay rate,  $1/\tau$ . If the gain profile is homogeneously broadened, then the loss of  $\text{KrF}^*$  by stimulated emission is proportional to the laser intensity,  $I$ . The continuity equation for  $\text{KrF}^*$  is then

$$\frac{\partial N^*}{\partial t} = R_p - N^*/\tau - \sigma I N^*/h\nu \quad (2)$$

where  $\sigma$  is the cross section for stimulated emission.

The steady state population density is given by  $N^* = R_p / (1/\tau + \sigma I/h\nu)$ . In terms of the saturated gain,  $g = \sigma N^*$ , and the small signal gain,  $g_0 = R_p \sigma \tau$ , this becomes  $g = g_0(1 + I/I_s)$ . The laser saturation intensity,  $h\nu/\sigma\tau$ , is the intensity at which stimulated emission equals quenching.

#### 4.3 Optical Resonator

As discussed in the previous section, for the case of homogeneous laser transitions, the saturated gain coefficient  $g$  is related to the small signal gain coefficient  $g_0$  by  $g = g_0 / (1 + \xi_+ + \xi_-)$ , where  $\xi_+$  and  $\xi_-$  are the laser intensities for the  $+x$  and  $-x$  directions normalized to the saturation intensity. In addition to gain, the  $\text{KrF}$  laser medium contains several species which absorb at the laser frequency. This absorption is distributed

throughout the cavity and may also show saturation effects. The species which exhibit gain and absorption in the KrF laser are listed in Table VII along with their respective saturation intensities defined as  $I_s = h\nu/\sigma\tau$  where  $\sigma$  is the optical cross section for stimulated emission or absorption and  $\tau$  is the mean lifetime of the particle.

Table VII.	$\sigma (\text{\AA}^2)$	$\tau (\text{ns})$	$I_s (\text{MW/cm}^2)$	
KrF*	1	3.6	2.2	3 atm
Ar <sub>2</sub> <sup>+</sup>	0.3	2.8	9.5	5% Kr
Kr <sub>2</sub> <sup>+</sup>	0.15	2.8	19	0.17% F <sub>2</sub>
F <sup>-</sup>	0.085	2	47	20 A/cm <sup>2</sup>
F <sub>2</sub>	0.00015	-	-	

The growth of laser intensity in the +x direction is governed by the equation,

$$\frac{1}{\xi_+} \frac{\partial \xi_+}{\partial x} = \frac{g_0}{1 + \xi_+ + \xi_-} - \sum_n \frac{\alpha_n}{1 + (\xi_+ + \xi_-) \frac{I_s}{I_n}} \quad (3)$$

where  $I_s$  is the saturation intensity for stimulated emission and  $I_n$  is the saturation intensity for the  $n^{\text{th}}$  absorbing species. Since the gain and absorption are isotropic  $\frac{1}{\xi_+} \frac{\partial \xi_+}{\partial x} = -\frac{1}{\xi_-} \frac{\partial \xi_-}{\partial x}$  and consequently  $\xi_+ \xi_- = \text{const} = \xi_0$ . Using this expression to relate  $\xi_-$  to  $\xi_+$  in Equation (3) we have, dropping the pluses,

$$\frac{1}{\xi} \frac{\partial \xi}{\partial x} = \frac{g_0}{1 + \xi + \xi_0^2/\xi} - \sum_n \frac{\alpha_n}{1 + (\xi + \xi_0^2/\xi) \frac{I_s}{I_n}} \quad (4)$$

If the cavity is defined by a perfect reflector at  $x = 0$  and a partial with reflectivity  $R$  at  $x = L$ , then  $\xi(0) = \xi_0$  and  $\xi(L) = \xi_0/\sqrt{R}$ . When Equation (4) is integrated from  $x=0$  to  $x=L$ , an expression relating  $\xi_0$ ,  $R$ ,  $g_0$ , and  $\alpha_n$

is obtained in principle. Then the laser output intensity is given by

$$(1 - R) \xi(L) = \xi_0 (1 - R)/\sqrt{R}.$$

In practice a simple closed-form solution to Equation (4) is only obtained if we approximate the distributed absorption as a lumped loss,  $a$ , in the output mirror. Integrating Equation (4) without the absorption term we obtain,

$$(\xi - \xi_0) + \ln(\xi/\xi_0) - \xi_0^2 \left( \frac{1}{\xi} - \frac{1}{\xi_0} \right) = g_0 x \quad (5)$$

Evaluating this at  $x = L$  with the boundary condition  $\xi(L) = \xi_0/\sqrt{R}$  gives,

$$(1 - R) \xi_0/\sqrt{R} = g_0 L - \ln \frac{1}{R} \quad (6)$$

The output intensity, defined as  $I_{out} = (1 - R - a) \xi(L) I_s$ , is then

$$I_{out} = I_s \frac{t}{a + t} \left( g_0 L - \ln \frac{1}{R} \right) \quad (7)$$

where  $t = 1 - R - a$  is the transmissivity of the output mirror.

We now define the extraction efficiency,  $\eta_c$ , as the ratio of actual output intensity to the intensity which would be obtained if every  $\text{KrF}^*$  generated in the cavity resulted in a photon leaving the output mirror. This maximum intensity is  $I_{max} = R_p V h \nu / A = g_0 L I_s$ , where  $R_p$  is the generation rate per unit volume of  $\text{KrF}^*$ . The extraction efficiency from Equation (7) is then

$$\eta_c = \frac{t}{a + t} \left( 1 - \frac{1}{g_0 L} \ln \frac{1}{R} \right) \quad (8)$$

In the KrF laser, the approximation of lumped losses at the mirrors is not very good, since the round trip absorption,  $a$ , often approaches unity and the resulting transmissivity,  $t$ , may go negative. Furthermore, the threshold gain derived from Equation (8) is independent of the absorption, a result which is clearly unphysical if the absorption is distributed. For if gain equals absorption, the medium will certainly not lase even though Equation (8) says it will if we chose the right reflectivity.

An approximation which yields more viable results in the presence of large absorption losses is to assume that the intracavity intensity,  $I = (\xi_+ + \xi_-) I_s$ , is constant, independent of  $x$ . Equation (4) can now be integrated readily to obtain,  $\ln(\xi/\xi_0) = (g - \alpha)x$ , where  $g$  and  $\alpha$  are the saturated gain and absorption respectively. Applying the previous boundary condition at  $x = L$  yields

$$\frac{1}{2L} \ln \frac{1}{R} = g - \alpha = \frac{g_0}{1 + I/I_s} - \sum_n \frac{\alpha_n}{1 + I/I_n} \quad (9)$$

After multiplying both sides by  $c$ , this equation says that the rate at which photons are being extracted from the cavity is equal to the difference between the rate at which they are produced and the rate at which they are absorbed. The output intensity is just the product of the extraction rate and the number of photons in the cavity divided by the area of the output aperture,  $A$ , i. e.

$$I_{\text{out}} = \frac{c}{2L} \ln \frac{1}{R} \cdot \frac{IV}{ch\nu} \cdot \frac{1}{A} \cdot h\nu = \frac{I}{2} \ln \frac{1}{R} \quad (10)$$

If  $I_n \gg I_s$  (see Table VII) then  $\alpha \sim \sum_n \alpha_n$  and Equation (9) can be solved for  $I$  directly. Thus,

$$I = I_s \left( \frac{g_0}{\alpha + \frac{1}{2L} \ln \frac{1}{R}} - 1 \right) \quad (11)$$

and the output intensity is therefore,

$$I_{\text{out}} = \frac{I_s}{2} \left( \ln \frac{1}{R} \right) \left( \frac{g_0}{\alpha + \frac{1}{2L} \ln \frac{1}{R}} - 1 \right) \quad (12)$$

The extraction efficiency analogous to Equation (8) is

$$\eta_c = \frac{1}{2L} \left( \ln \frac{1}{R} \right) \left( \frac{1}{\alpha + \frac{1}{2L} \ln \frac{1}{R}} - \frac{1}{g_0} \right) \quad (13)$$

This expression has been compared with the numerical solution of Equation (4) and was found in good agreement for values of  $R$  down to 30% independent of  $\alpha$ . In contrast to Equation (8) the threshold gain is now a



function of the distributed absorption. If there is also some lumped absorption,  $a$ , in the optical components, this can be taken care of as before and the final expression for extraction efficiency becomes,

$$\eta_c = \frac{t}{a+t} \frac{1}{2L} \left( \ln \frac{1}{R} \right) \left( \frac{1}{\alpha + \frac{1}{2L} \ln \frac{1}{R}} - \frac{1}{g_o} \right) \quad (14)$$

If  $a \ll t$  the optimum reflectivity is given by

$$\frac{1}{2L} \ln \frac{1}{R} = \sqrt{\alpha g_o} - \alpha \quad \text{and the} \quad (15)$$

maximum extraction efficiency is, from Equation 14 ,

$$\eta_c^{\max} \sim \left( 1 - \sqrt{\frac{\alpha}{g_o}} \right)^2 \quad (16)$$

This function is plotted in Figure 32.

In a practical device the mirrors cannot be placed directly adjacent to the gain region. Because of the electric field applied to the discharge, the mirrors must be set back a distance at least equal to the electrode separation. Alternatively, windows may be used to contain the laser gas and the mirrors mounted externally. We must then define several different lengths and modify our expression for the extraction efficiency and optimum reflectivity. Let  $L$  remain the mirror separation and define  $l_s$  as the gain length and  $l_n$  the length containing the  $n^{\text{th}}$  absorbing species. Then Equation (14) becomes

$$\eta_c = \frac{t}{a+t} \frac{1}{2} \left( \ln \frac{1}{R} \right) \left( \frac{1}{\sum_n \alpha_n l_n + \frac{1}{2} \ln \frac{1}{R}} \right) - \frac{1}{g_o l_s} \quad (17)$$

and the optimum reflectivity is,

$$\frac{1}{2} \ln \frac{1}{R} = \sqrt{g_o l_s \sum_n \alpha_n l_n} - \sum_n \alpha_n l_n \quad (18)$$

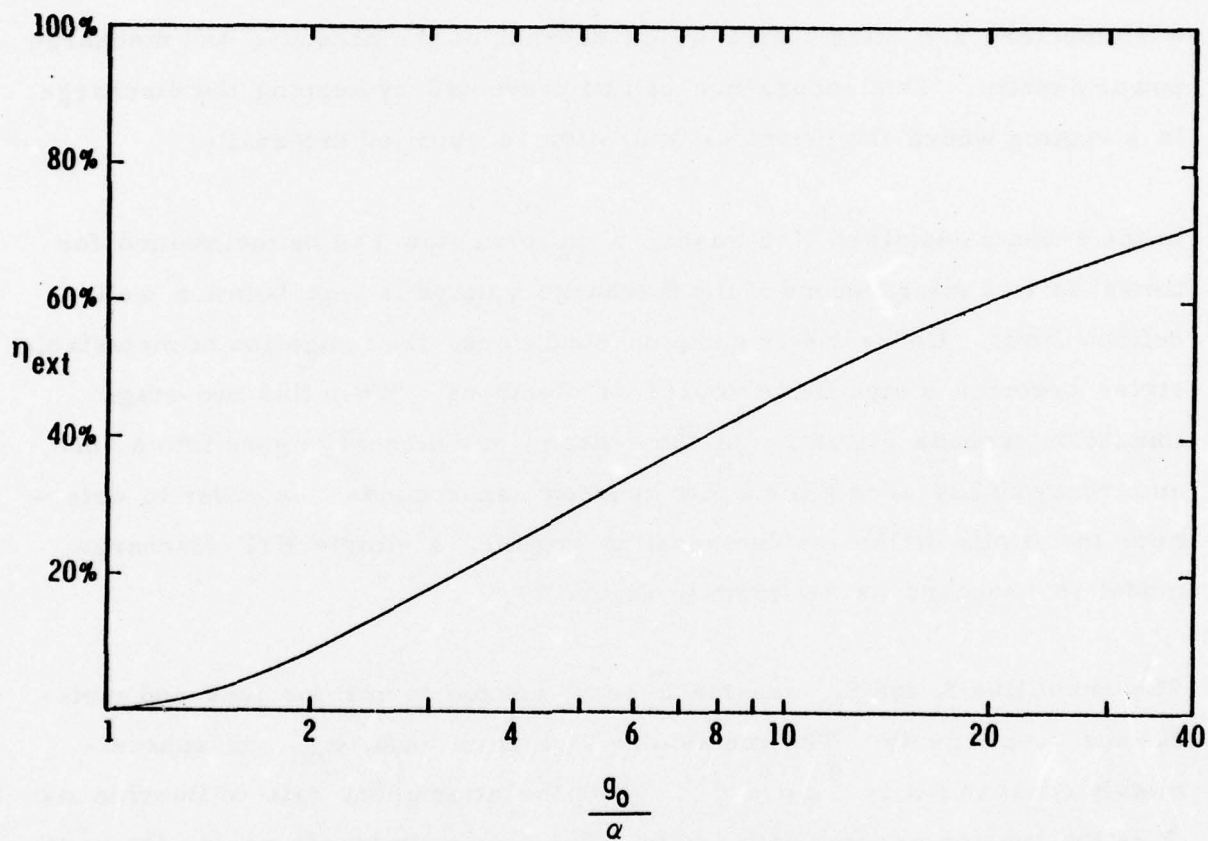


Figure 32. Laser Extraction Efficiency

## 5.0 SCALING CONSIDERATIONS

### 5.1 Discharge Stability

The glow discharge, which is an effective excitation technique for a variety of gas lasers, is unstable at high pressures unless sustained by an external ionization source. In the self-sustained mode, the initial glow collapses into a filamentary arc after a time which depends on the pressure and discharge power density. This occurrence can be prevented by keeping the discharge in a regime where the principal ionization is supplied externally.

In the e-beam sustained KrF laser, a uniform glow can be maintained for times up to a microsecond if the discharge voltage is kept below a well-defined limit. Under heavy pumping conditions, the ionization of metastable states becomes a significant source of electrons. When this two-stage ionization exceeds ionization by the e-beam, the discharge goes into a volume runaway and arcs after a few hundred nanoseconds. In order to determine the limits of the stable operating regime, a simple KrF discharge model is proposed as set forth in Figure 33.

The quantities  $S_i$  and  $S_m$  are the e-beam source terms for ions and metastables respectively. The metastable ionization rate,  $k_{mi}$ , is approximately equal to  $6 \times 10^{-8} \text{ cm}^3 \text{ sec}^{-1}$ .  $\beta$  is the attachment rate to fluorine and  $\gamma$  is the ion-ion recombination rate. The continuity equations for the metastables can be lumped together with a single density,  $m$ , because the quenching rate,  $Q$ , and ionization rate,  $k_{mi}$ , are fairly independent of species. The metastable production rate,  $k_m$ , is then a weighted sum of the production rates for  $\text{Ar}^*$  and  $\text{Kr}^*$ . This rate is a strong function of  $E/N$  and is plotted in Figure 34 for several values of fractional ionization  $n/N$ .

Since the time constant for the external circuit,  $\sqrt{LC} \sim 200\text{-}500 \text{ ns}$ , is typically large compared to that for equilibrium of the ion and metastable

Plasma Kinetics:

$$\frac{\partial n}{\partial t} = S_i + k_{mi} mn - \beta F_2 n$$

$$\frac{\partial F_-}{\partial t} = \beta F_2 n - \gamma_i F_- (n + F_-)$$

$$\frac{\partial m}{\partial t} = S_m + k_m Nn - k_{mi} mn - QF_2 M$$

Discharge Circuit

$$L \frac{d^2 I}{dt^2} + \frac{dV}{dt} + I/C = 0$$

$$I = eAnv_e + \frac{V}{R}$$

Figure 33. Simple KrF Laser Model



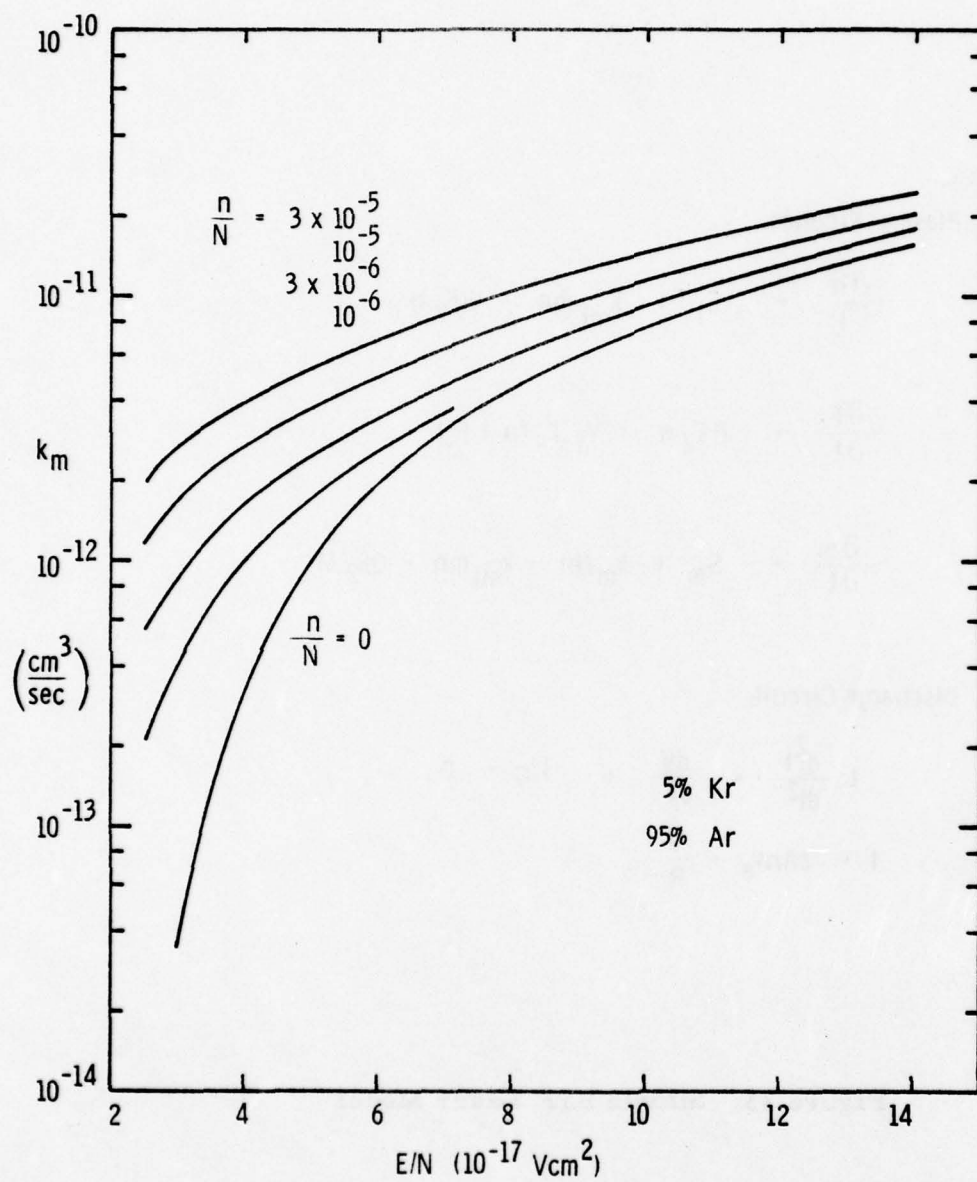


Figure 34. Metastable Production Rate

species densities, the equations for the latter can be solved in the quasi-steady-state approximation. The stability of the steady-state solution is then found by applying a small perturbation with time dependence proportional to  $\exp(-i\omega t)$  and looking for positive imaginary eigenvalues of  $\omega$ . When this is done for the equations in Figure 33, the resulting linearized system for the perturbation on electron and metastable densities is,

$$(i\omega + k_{mi}m_o - \beta F_2) \tilde{n} + k_{mi}n_o \tilde{m} = 0 \quad (19)$$

$$(k_m N - k_{mi}m_o) \tilde{n} + (i\omega - k_{mi}n_o - QF_2) \tilde{m} = 0 \quad (20)$$

The eigenvalues are then solutions of

$$\omega^2 + i\omega \left( \frac{S_i}{n_o} + QF_2 + k_{mi}n_o \right) - \frac{S_i}{n_o} QF_2 - k_{mi}n_o (\beta F_2 - k_m N) = 0 \quad (21)$$

Thus  $2\omega = -b \pm \sqrt{b^2 - 4c}$ , where  $b$  is the coefficient of  $\omega$  in Equation 21, and  $c$  is the constant term. Since  $b$  is positive imaginary,  $\omega$  will have a positive imaginary part only if  $c > 0$ . The stability requirement is then,

$$\frac{S_i}{n_o} QF_2 > k_{mi}n_o (k_m N - F_2) \quad (22)$$

or

$$m_o < m_p = 1/2 \left( \frac{\beta F_2}{k_{mi}} + \frac{S}{QF_2} \right), \text{ where } S = S_i + S_m$$

In the limit of low e-beam current density, the second term in parentheses is negligible and the condition for stability reduces to that found previously.<sup>32</sup> In its present form the maximum metastable density is a function of e-beam source strength.

The stability criterion as presented in Equation (22) is not very useful in defining a practical operating regime since it involves the steady-state metastable density,  $m_o$ . In order to express this in terms of experimentally definable parameters, we solve the steady-state equations for  $m_o$ . From

Figure 33,  $n_o = S_i / (\beta F_2 - k_{mi} m_o)$ . Using this in the equation for  $m$ , we arrive at a quadratic equation for  $m_o$  with solutions,

$$m_o = m_p \pm \sqrt{m_p^2 - m_c^2}, \quad (23)$$

where

$$m_c^2 = (S_m \beta F_2 + S_i k_{mi} N) / Q F_2 k_{mi}$$

If  $m_c < m_p$ , then two real solutions exist, one of which,  $m_o < m_p$ , is stable and the other,  $m_o > m_p$ , is unstable. The stable solution is the one which is reached first as  $m$  increases from zero. Stability will be maintained as long as  $m_c < m_p$  is satisfied.

A new stability criterion can now be written in the form of an upper limit on  $E/N$  or discharge voltage, i.e

$$k_m \left( \frac{E}{N}, \frac{n}{N} \right) < \frac{k_{mi} Q F_2}{S_i N} \left[ \frac{1}{4} \left( \frac{\beta F_2}{k_{mi}} + \frac{S}{Q F_2} \right)^2 - \frac{S_m \beta}{Q k_{mi}} \right] \quad (24)$$

The term on the right side of the inequality is only weakly dependent on  $E/N$ . The value of  $n/N$  on the left is the steady-state fractional ionization at the point where  $m_o = m_p$  and  $n_o = 2S_i / (\beta F_2 - k_{mi} S / Q F_2)$ . For a given e-beam current, gas density,  $N$ , and fluorine density,  $F_2$ , we can use Figure 34 and Equation(24) to establish the critical value of  $E/N$  above which the discharge current will run away. Experimentally, with the current rise limited by circuit inductance, this runaway is seen as a drop in discharge impedance and a cessation of lasing.

In Figure 35 the critical value of  $E/N$  is plotted as a function of e-beam power density for several values of total pressure and fluorine concentration. The experimental points are taken from the current and voltage waveforms obtained on the 0.1  $\ell$  device described in Section 3.2. The functional dependence of  $E/N$  on  $P_{eb}$  is roughly  $E/N \propto P_{eb}^{-0.5}$  for the conditions indicated. The dependence of  $E/N$  on  $F_2$  concentration is

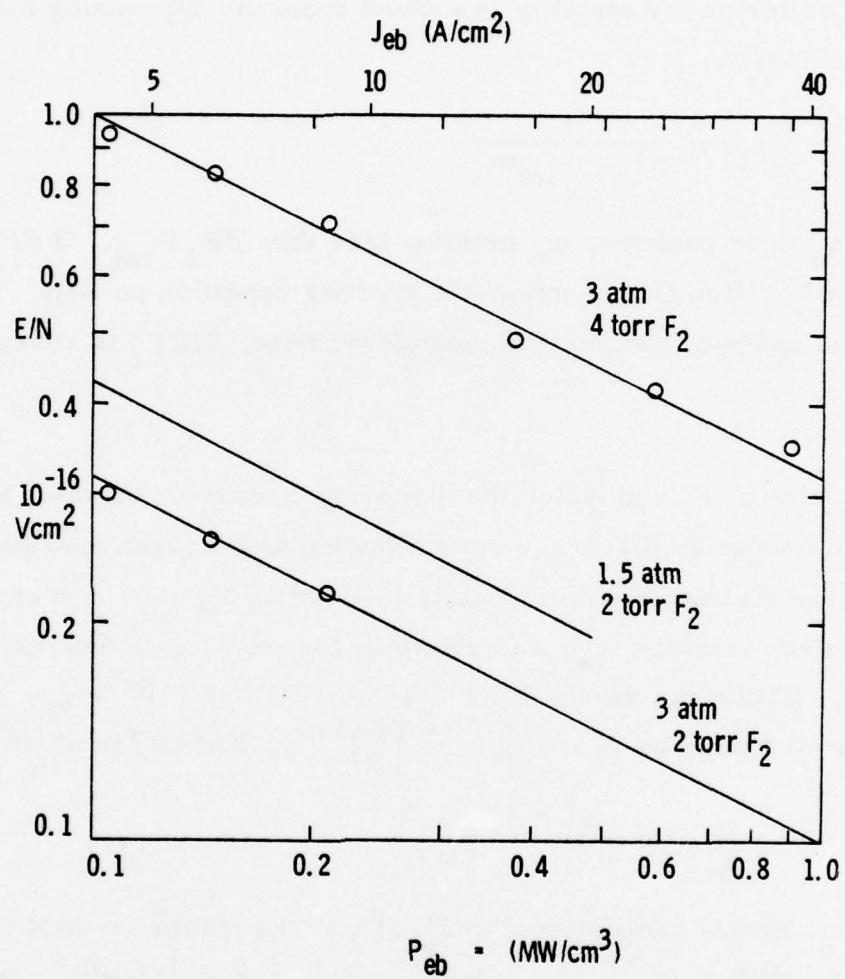


Figure 35. Maximum  $E/N$  vs E-Beam Density



likewise  $E/N \propto F_2^{1.7}$  and on total number density  $E/N \propto N^{-0.9}$ . These expressions are only approximately valid within the range of parameters given in Figure 35.

A subsidiary criterion for stability is evident from the expression for steady-state electron density, i.e.

$$n_o = \frac{S_i}{\beta F_2 - k_{mi} m_o} \quad (25)$$

In order for  $n_o$  to be positive,  $m_o$  must be less than  $\beta F_2 / k_{mi}$ . If  $S/QF_2 > \beta F_2 / k_{mi}$ , then Equation (25) becomes the limiting condition on  $E/N$ . However, over the range of parameters considered here,  $S/QF_2$  is always less than  $\beta F_2 / k_{mi}$ .

Knowing the value of  $E/N$  at which the discharge becomes unstable, we can determine the maximum discharge power loading under given operating conditions. The discharge power density is given by  $P_d = J \cdot E = env_e E$ . The electron drift velocity,  $v_e$ , was shown in Figure 27 as a function of  $E/N$  and  $n/N$ . Within the range,  $1 \text{ Td} < E/N < 10 \text{ Td}$  and  $10^{-6} < \frac{n}{N} < 10^{-5}$ ,  $v_e$  can be approximated by  $v_e = b \left( \frac{n}{N} \right)^{0.2} \left( \frac{E}{N} \right)^{0.4}$ . Then  $P_d$  is given by

$$P_d = ebN^2 \left( \frac{n}{N} \right)^{1.2} \left( \frac{E}{N} \right)^{1.4} \quad (26)$$

For  $m_o \ll m_p$ ,  $n/N$  is proportional to  $J_{eb}/F_2$ . The maximum  $E/N$  is proportional to  $J_{eb}^{-0.5} F_2 N^{-0.9}$ . Therefore  $P_d \propto J_{eb}^{0.5} F_2^{1.2} N^{0.7}$ . Writing this in terms of the e-beam power density  $P_{eb} \sim J_{eb} N$ , we have  $P_d \propto P_{eb}^{0.5} F_2^{1.2} N^{0.25}$ .

The maximum discharge power density is proportional to the square root of the e-beam power deposition. This means that the power enhancement factor,  $P_d/P_{eb}$ , is smaller at higher e-beam current densities. It is larger at higher  $F_2$  concentrations and, in a given mixture, at higher total pressures.

For overall system efficiency, it is desirable to have  $P_d/P_{eb}$  as large as possible. In this respect then it is better to operate at low beam currents and high  $F_2$  and total pressures. The limitation in going to low e-beam current densities is that as the total power is reduced, the ratio of small signal gain to absorption is less and extraction efficiency becomes poor, Figure 32. The limitation on fluorine concentration arises from quenching of the  $KrF^*$  state and absorption by  $F_2$  and  $F_2^-$ . At higher pressures there is more three-body quenching of  $KrF^*$  and increased formation of the trimers,  $Ar_2F^*$ ,  $ArKrF^*$  and  $Kr_2F^*$  by interception of energy channels leading to  $KrF^*$ . There is therefore an optimum choice of the parameters  $N$ ,  $F_2$ , and  $J_{eb}$ , which will give the highest overall efficiency and laser output.

## 5.2 Scaling of the KrF Laser

The KrF laser has the greatest potential of all other candidates for scaling to very high average powers in the near ultraviolet. The highest specific energy (30 J/l) and efficiency (10%) to date have been demonstrated in a small device (0.12 l) with an e-beam sustained discharge. In larger devices, however, discharge loading has not been nearly as effective and in most cases has been abandoned as a viable pumping technique. We believe that efficient discharge pumping in large devices can be achieved and that this represents the best alternative for a reasonably sized high average power laser.

We have undertaken a systematic study of the electron kinetics, discharge stability, e-beam deposition, and optical extraction in order to determine the scalability of the KrF laser and to assess the relative merits of e-beam versus discharge pumping. We find that discharge power loading is limited by the nonuniformity of e-beam deposition and by the ability of the external circuit to couple energy into a low-impedance load. If the energy deposition is made uniform through the use of opposed e-beams and the device is operated at low beam currents to maximize the discharge impedance, then an

extracted laser energy of 45J/l can be achieved with 8% efficiency. This is about a factor of three more energy than could be extracted with an e-beam alone. The implications are that a much smaller device can be built for a given average power with all the associated savings in optics, size and gas handling equipment.

The maximum discharge power loading,  $P_d$ , consistent with stable, long-pulse operation is proportional to the square root of the e-beam power density,  $P_e$ . This relationship has been derived from a discharge stability analysis (Section 5.1) and has been confirmed experimentally. The stability criterion for discharge pumping is then,

$$P_d < \gamma P_e^{1/2} \quad (27)$$

For the gas mixture 94.8% Ar 5% Kr 0.17%  $F_2$  at a total pressure of 3 atm, the constant,  $\gamma$ , is equal to 1.3 when  $P_d$  and  $P_e$  are given in  $MW/cm^3$ . The above condition must be satisfied at every point in the discharge or two-stage ionization will lead to volume runaway and eventual arcing.

Another condition which must be satisfied in the discharge is current continuity. Near the center of large planar electrodes, this implies constant current density along a field line, i.e.

$$J_d = ev_e \left( \frac{E}{N}, \frac{n}{N} \right) = \text{const} \quad (28)$$

where  $E$  is the electric field strength and  $N$  is the gas density. Since the electron density,  $n$ , is controlled by the e-beam deposition which varies with distance from the foil, the electric field must compensate by changing the electron drift velocity,  $v_e$ . Within the range,  $1 \text{ Td} < E/N < 10 \text{ Td}$  and  $10^{-6} < n/N < 10^{-5}$ ,  $v_e$  can be approximated by,

$$v_e = b \left( \frac{n}{N} \right)^{0.2} \left( \frac{E}{N} \right)^{0.4} \quad (29)$$



The current density is then given by,

$$J_d = eNb \left( \frac{n}{N} \right)^{1.2} \left( \frac{E}{N} \right)^{0.4} \quad (30)$$

from which it is clear that along a field line  $E/N$  must vary inversely as the cube of  $n/N$  in order to keep the current density constant.

Monte Carlo simulation studies and experimental measurements of the e-beam energy deposition in gases show that the deposition falls off more or less linearly away from the foil for the range of beam energies and foil thicknesses considered here. This spatial dependence can be written as,

$$P_e(x) = P_{e0} [1 + (r-1)x/d] \quad (31)$$

where  $r$  is the ratio of the power density at a distance  $d$  from the foil to the power density at the foil. The source density,  $S$ , for generating electrons in the gas is related to the e-beam power density by  $S = P_e/W_i$ , where  $W_i$  is the energy dissipated in creating an electron-ion pair. (For argon  $W_i = 26.2$  eV). Since the principal loss of electrons is by attachment to fluorine, the electron density is given by,

$$n = S/\beta F_2 = P_e/\beta F_2 W_i \quad (32)$$

where  $\beta$  is the attachment coefficient and  $F_2$  is the fluorine density.

The discharge power density is given by,

$$P_d = NJ_d E/N \quad (33)$$

and since  $J_d$  is constant along a field line,  $P_d$  varies directly as  $E/N$ . From Equations 30 and 32 then, we see that  $P_d$  must vary inversely as the cube of  $P_e$  (Figure 36), or

$$P_d(x) = c [1 + (r-1)x/d]^{-3} \quad (34)$$



$$J = en_e v_e \propto n_e^{1.2} \left( \frac{E}{N} \right)^{0.4} = \text{const}$$

Then since  $P_d = J \cdot E \propto \frac{E}{N}$

and  $P_{eb} \propto n_e$

$$P_d(z) \propto P_{eb}^{-3}$$

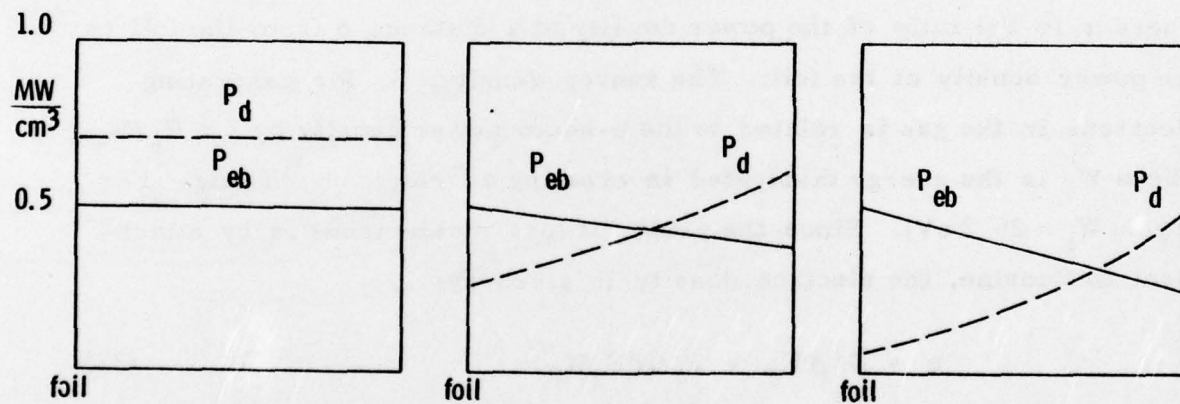


Figure 36. Discharge Current Continuity

The constant  $c$  will now be chosen so that the stability criterion, Equation (27), is satisfied throughout the discharge. It is clear from Equation (34) that the condition is most likely to be violated at  $x = d$ . Therefore, we set  $P_d(d) = \gamma P_e^{1/2}(d)$  or  $cr^{-3} = \gamma r^{1/2} P_{eo}^{1/2}$  so that  $c$  is given by  $c = \gamma r^{7/2} P_{eo}^{1/2}$ . The average e-beam and discharge power densities can now be found by integrating Equations (31) and (34) over  $x$  from 0 to  $d$ . Thus,

$$\bar{P}_e = P_{eo}(1+r)/2 \quad (35)$$

and

$$\bar{P}_d = \gamma P_{eo}^{1/2} r^{3/2} (1+r)/2 \quad (36)$$

If the discharge power is supplied by a simple capacitive discharge circuit, where maximum power is reached at the end of the e-beam pulse, then the discharge power averaged over time is just half of that given in Equation (36). The total energy dissipated in the laser is then,

$$\epsilon_{in} = (\bar{P}_e + \bar{P}_d/2) \tau_p \quad (37)$$

where  $\tau_p$  is the pulse length.

The quantum efficiency for converting e-beam energy into excited KrF is  $h\nu(1 + \delta_e)/W_i = 25\%$ , where  $\delta_e$  is the fraction of excited states produced for every ion pair. (For argon  $\delta_e = 0.29$ ). The quantum efficiency for converting discharge energy into KrF\* states is 36% (see Section 4.1). The actual conversion efficiencies are somewhat lower due to formation of trimers and the loss of ArF\* to quenching and spontaneous emission. In an optimized gas mixture, conversion efficiencies of  $\eta_e = 20\%$  and  $\eta_d = 25\%$  can readily be achieved. These values are independent of input power density. The average production rate of KrF\* per unit volume,  $R_p$ , can now be written,

$$R_p = (\eta_e P_{eo} + \eta_d \gamma P_{eo}^{1/2} r^{3/2} / 2) (1+r) / 2h\nu \quad (38)$$

Since the ground state of  $\text{KrF}^*$  is dissociative, the small-signal gain is given by  $g_o = \sigma N^* = \sigma R_p \tau$ , where  $\sigma$  is the cross section for stimulated emission and  $\tau$  is the total  $\text{KrF}^*$  lifetime. Another way of writing this relation is  $g_o = R_p h\nu / I_s$ , where  $I_s = h\nu / \sigma \tau$  is the saturation intensity. Using a spontaneous emission lifetime of  $9 \text{ ns}$ <sup>33</sup>, a stimulated emission cross section of  $1.9 \text{ \AA}^2$  and the published fluorine and three-body quenching rates<sup>34</sup> of  $\text{KrF}^*$ , the saturation intensity for the mixture 94.8% Ar 5% Kr 0.17%  $\text{F}_2$  at 3 atm is  $2.6 \text{ MW/cm}^2$ . The expression for the average small-signal gain is then,

$$g_o = (\eta_e P_{eo} + \eta_d \gamma P_{eo}^{1/2} r^{3/2})(1+r) / 2I_s \quad (39)$$

Since the discharge power density is greatest where the e-beam power density is at least, the sum of the two is fairly constant and the error in using averaged quantities is minimal.

The laser output intensity is given in terms of the small-signal gain, the gain length,  $l$ , the mirror reflectivity,  $R$ , and the absorption in the laser medium,  $\alpha$ , by the expression, (see Section 4.3),

$$I_{\text{out}} = \frac{I_s}{2} \ln \frac{1}{R} \left( \frac{g_o}{\alpha + \frac{1}{2l} \ln \frac{1}{R}} - 1 \right) \quad (40)$$

This expression has been compared with an exact numerical solution of the cavity equations, and was found in good agreement for values of  $R$  down to 30%.

The maximum output intensity corresponding to complete extraction of all laser photons is

$$I_{\text{max}} = R_p h\nu V/A = g_o l I_s \quad (41)$$



so the extraction efficiency can be defined as,

$$\eta_{\text{ext}} = I_{\text{out}}/I_{\text{max}} = \frac{1}{2l} \ln \frac{1}{R} \left( \frac{1}{\alpha + \frac{1}{2l} \ln \frac{1}{R}} - \frac{1}{g_0} \right) \quad (42)$$

The optimum reflectivity is found from Equation (42) to be

$$\frac{1}{2l} \ln \frac{1}{R} = \sqrt{\alpha g_0} - \alpha \quad (43)$$

which corresponds to a maximum extraction efficiency of

$$\eta_{\text{ext}}^{\text{max}} = \left( 1 - \sqrt{\frac{\alpha}{g_0}} \right)^2 \quad (44)$$

The extracted laser energy density  $\epsilon_{\text{out}}$  can now be written as

$$\epsilon_{\text{out}} = \eta_{\text{ext}} R_p h\nu \tau_p \quad (45)$$

Absorption in the laser medium is made up of two types: 1) static absorption by molecular fluorine and 2) transient absorption due to  $F^-$ , positive molecular ions, and possibly excited electronic states. Our absorption measurements show that the dominant transient absorption is due to the ions,  $F^-$ ,  $Kr_2^+$  and  $Ar_2^+$ . Since the ions are lost by recombination, their population is proportional to the square root of the e-beam power density. We can therefore write,

$$\alpha = \sqrt{cP_e/W_i} + \sigma_{F_2}[F_2] \quad (46)$$

where  $c$  is a constant determined experimentally to be  $4 \times 10^{-28}$  cm-sec and  $\sigma_{F_2} = 1.5 \times 10^{-20}$  cm<sup>2</sup>.

The e-beam pulse length is chosen so that  $\tau_p J_e = 10 \mu\text{coul/cm}^2$ . This value has been found to be an upper limit for the consistent operation of a single shot e-beam device without foil damage. This limitation also points out the advantage of operating at the highest pressure consistent



with good laser efficiency, since the e-beam energy deposition,  $P_e \tau_p$ , is now independent of the current density but proportional to gas density. We have chosen our test case at 3 atm, because this pressure has resulted in efficient laser operation in small devices. The reason that lower pressures have been found to give higher output in large devices is because of poor e-beam penetration at high pressures. The nonuniformity of e-beam deposition also limits the discharge energy loading in large devices, as we shall see below.

We now have all the information necessary to determine the extracted laser energy density from Equation (45). This is plotted as a function of  $P_{eo}$  in Figure 37 for the mixture 94.8% Ar 5% Kr 0.17%  $F_2$  at 3 atm. The corresponding e-beam current density is given on the upper scale. The curves show that a high extracted laser energy is possible at low e-beam current densities if the e-beam deposition is uniform. The uniformity becomes more critical the smaller the value of  $P_{eo}$ . When  $r=0$  there is no benefit from discharge pumping at all, since the discharge is always unstable.

The small-signal gain and absorption for the same gas mixture are plotted in Figure 38 as a function of e-beam power density. The horizontal line at  $0.24\% \text{ cm}^{-1}$  is the absorption due to 4 Torr of fluorine with the factor  $L/l = 1.2$  taken into account. ( $L$  is the distance between the laser mirrors, or windows, which is filled with fluorine. The value 1.2 is required to ensure electrical isolation of the electrodes from the mirror mounts.) Most of the remaining absorption is due to the ions  $F^-$ ,  $Ar_2^+$  and  $Kr_2^+$  which are proportional to  $P_{eo}^{1/2}$ . The measurements by AVCO at the same pressure in a slightly different mix are shown for comparison. Their values,  $A$ , for the transient absorption at 1.5 and 6  $\text{A/cm}^2$  are added to our baseline at  $0.24\% \text{ cm}^{-1}$ . The small-signal gain is seen to increase faster than the absorption in going to harder pumping.

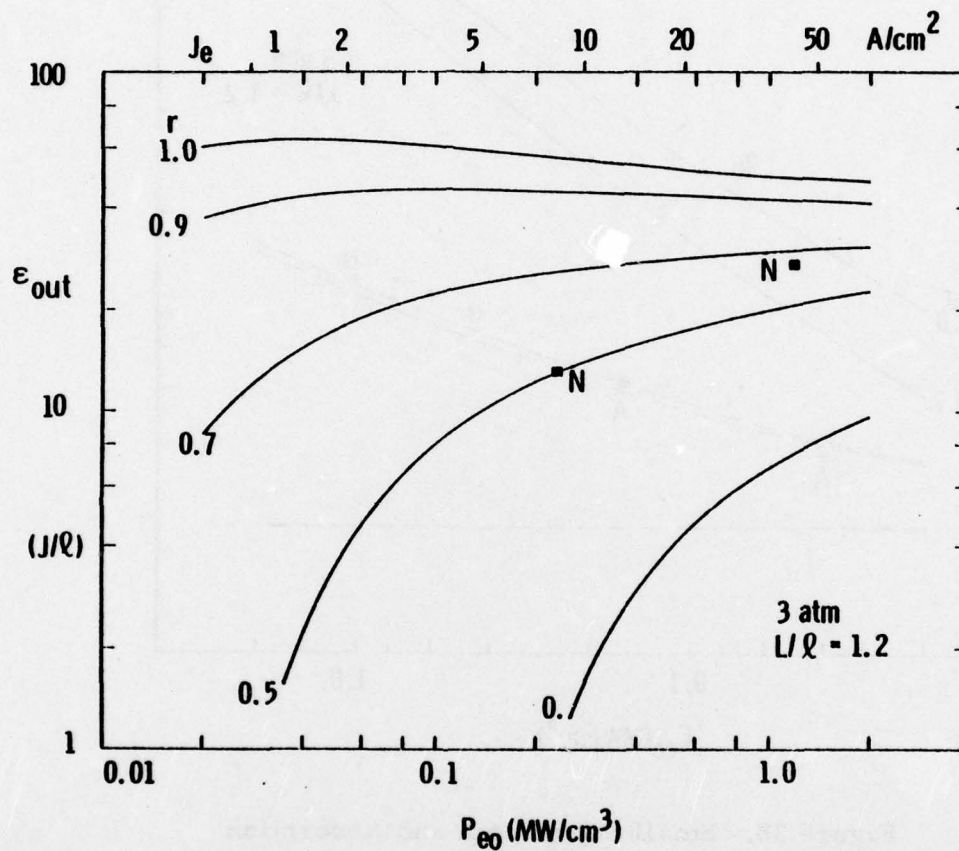


Figure 37. Specific Energy (e-beam + discharge)

(■) Experimental data obtained on  
two Northrop devices

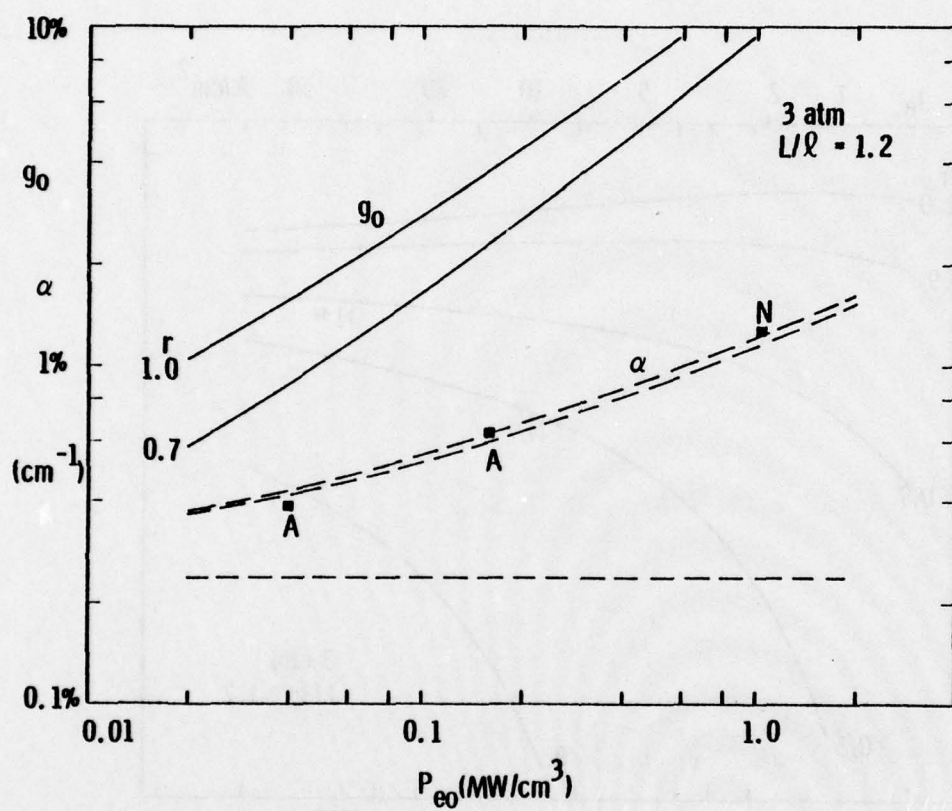


Figure 38. Small-Signal Gain and Absorption  
(e-beam + discharge)



From Equation (43) it is seen that, for a given small-signal gain and absorption, the optimum mirror reflectivity,  $R$ , is determined by the gain length,  $l$ . As the laser is increased in length, the optimum value of  $R$  is reduced. However, there is a minimum value of  $R$  below which the mode quality of the laser suffers due to superfluorescence. The minimum reflectivity is found experimentally to be about 20%. This condition sets a limit on the length of the laser given by,

$$l^{\max} = \frac{\ln(1/R_{\min})}{2(\sqrt{ag_0} - \alpha)} \quad (47)$$

Thus, as the input power density increases and the small-signal gain and absorption go up, the maximum length of the device is reduced. This is an important consideration in scaling to high pulse energies.

In Figure 39 the overall laser efficiency, maximum gain length and discharge enhancement factor are plotted as a function of e-beam power density. The discharge enhancement factor is defined as the ratio of energy deposited in the gas by the discharge to that deposited by the e-beam. It can be determined from Equations (35) and (36) as

$$\bar{P}_d / 2\bar{P}_e = \gamma_r^{3/2} / 2P_{eo}^{1/2} \quad (48)$$

The overall efficiency is an increasing function of  $P_{eo}$  since the small signal gain is increasing faster than the absorption. From this graph we can see that there is a tradeoff to be made between the size of a device and the operating efficiency. With a one meter gain length, an extracted energy of  $45 \text{ J/l}$  can be achieved at 8% efficiency with an e-beam current density of  $6 \text{ A/cm}^2$ . In contrast, a one meter laser pumped by an e-beam alone at  $12 \text{ A/cm}^2$  can deliver only  $11 \text{ J/l}$  at 8% efficiency (see Figures 40 and 41). The difficulty comes in achieving less than 10% variation in e-beam deposition in the field direction. We feel that the only way this can be done is with two opposed e-beams.



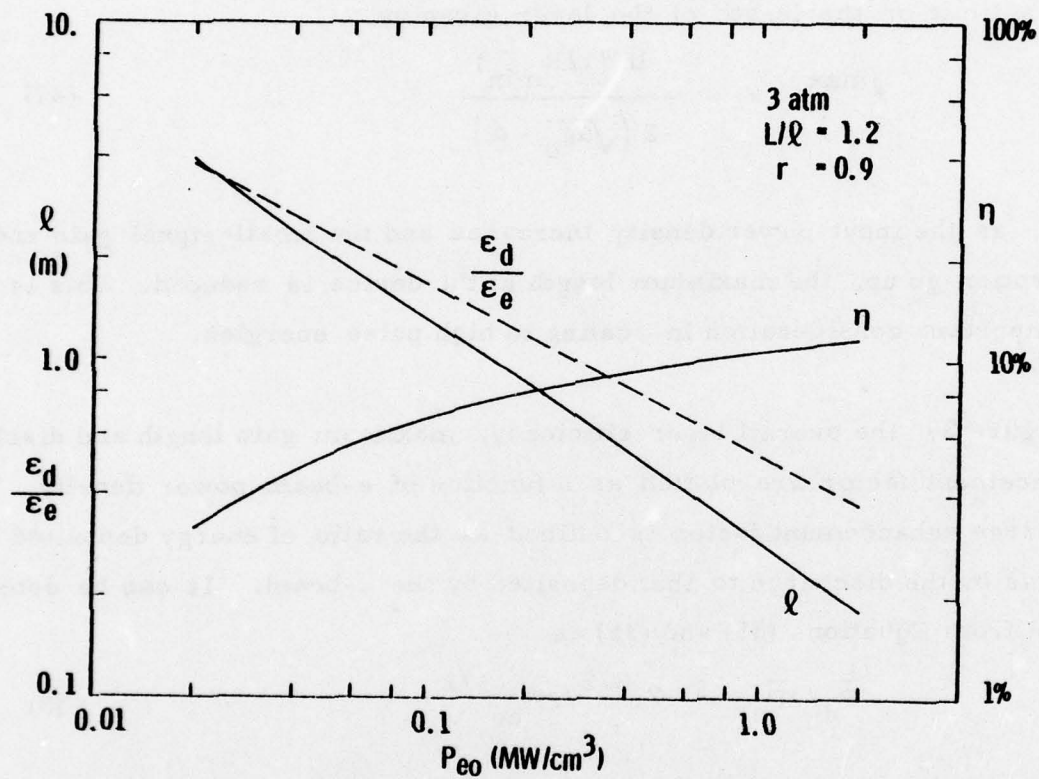


Figure 39. Maximum Gain Length and Efficiency  
(e-beam + discharge)

Some comparison runs with e-beam pumping only were made assuming uniform deposition ( $r = 1$ ) and  $L/l = 1$ . The extracted energy density is plotted in Figure 40 for 1.5 and 3 atm total pressure. Two conclusions may be drawn from these curves: 1) harder pumping works best at higher pressures and 2) the extracted energy always increases with pumping power. The best experimental results of Maxwell (2 atm), AVCO (1.7 atm) and Northrop are in good agreement with the predictions.

The maximum gain length and overall efficiency for an e-beam pumped  $\text{KrF}^*$  laser are shown in Figure 41. Again the tradeoff between device size and efficiency is clear. The lasers of Maxwell, AVCO and Northrop are seen to be very close to the limit of scalability. The only way to go to higher than 10 to 12 J/l without severely limiting the device size is through combined e-beam and discharge pumping with the uniform deposition achieved by opposing beams.

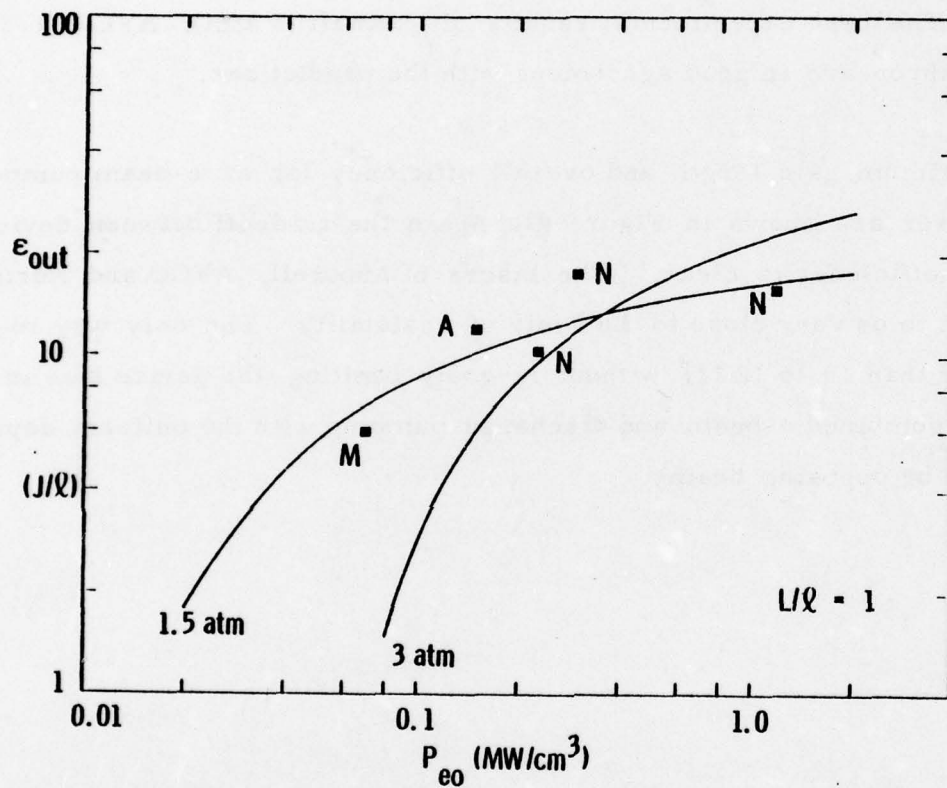


Figure 40. Specific Energy (e-beam only)

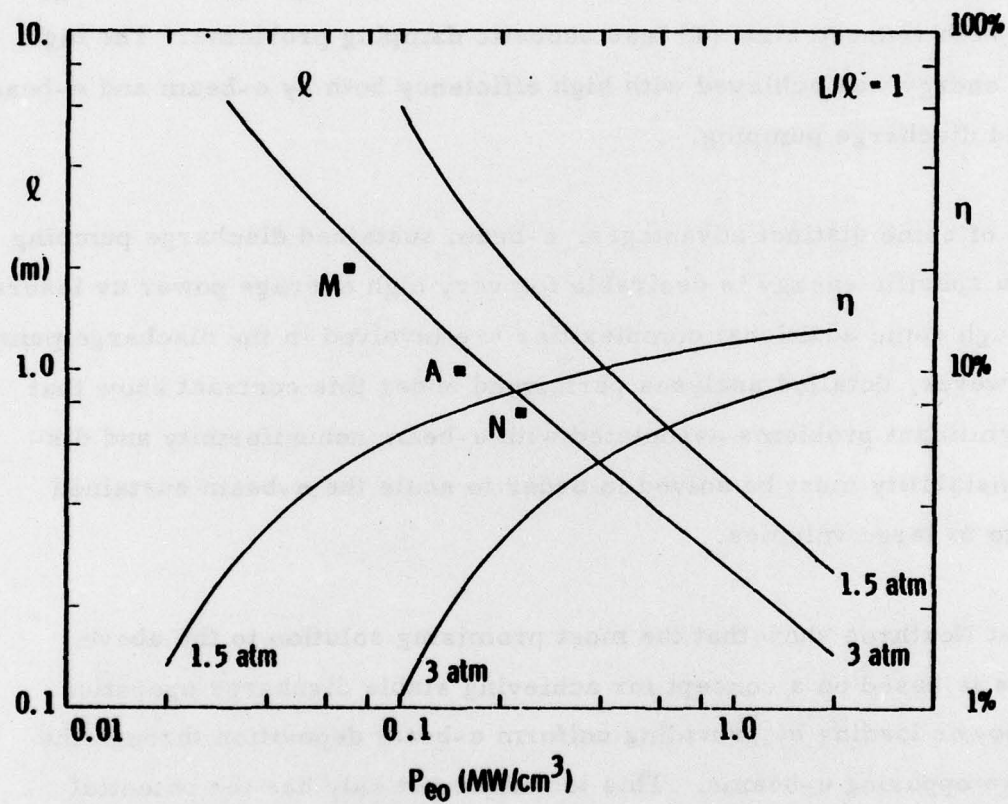


Figure 41. Maximum Gain Length and Efficiency  
(e-beam only)



## 6.0 CONCLUSIONS

As a result of the detailed investigations carried out under this contract, the great potential of rare gas halide lasers, particularly the krypton fluoride laser, is clearly established for the development of an efficient, high average power laser in the near ultraviolet. The attainment of specific energy as high as 30 J/liter, compared to the previously reported value of 10 J/liter, represents a significant advance since high specific energy leads to both reduced size and less acoustic damping problems. The high specific energy was achieved with high efficiency both by e-beam and e-beam sustained discharge pumping.

Because of some distinct advantages, e-beam sustained discharge pumping with high specific energy is desirable for very high average power uv lasers even though some additional complexities are involved in the discharge pumping. However, detailed analyses performed under this contract show that some significant problems associated with e-beam nonuniformity and discharge instability must be solved in order to scale the e-beam sustained discharge to large volumes.

Studies at Northrop show that the most promising solution to the above problems is based on a concept for achieving stable discharge operation at high power loading by providing uniform e-beam deposition through the use of two opposing e-beams. This technique not only has the potential for scaling to a volume of nearly 250 liters, but it may also lead to specific energy as high as 40 J/liter. Therefore, a proof of concept program is highly recommended for the experimental demonstration of the scaling potential of the discharge technique using two opposing e-beams.

## 7.0 REFERENCES

1. E. R. Ault, R. S. Bradford, Jr., and M. L. Bhaumik, Appl. Phys. Lett. 27, 413 (1975).
2. C. A. Brau and J. J. Ewing, Appl. Phys. Lett. 27, 435 (1975).
3. J. J. Ewing and C. A. Brau, Appl. Phys. Lett. 27, 350 (1975)
4. S. K. Searles and G. A. Hart, Appl. Phys. Lett. 27, 243 (1975).
5. R. S. Bradford, Jr., E. R. Ault, and M. L. Bhaumik, Electronic Transition Lasers, ed. J. I. Steinfeld (M.I.T. Press, Cambridge, 1975), p. 211.
6. R. S. Bradford, Jr., E. R. Ault, and M. L. Bhaumik, Appl. Phys. Lett. 27, 546 (1975).
7. J. J. Ewing and C. A. Brau, Appl. Phys. Lett. 27, 557 (1975).
8. M. L. Bhaumik, R. S. Bradford, Jr., and E. R. Ault, Appl. Phys. Lett. 28, 23 (1976).
9. J. E. Velazco and D. W. Setser, J. Chem. Phys. 62, 1990 (1975).
10. J. Tellinghuisen, A. K. Hays, J. M. Hoffman, and G. C. Tisone, J. Chem. Phys. 65, 4473 (1976).
11. J. G. Eden and S. K. Searles, Appl. Phys. Lett. 30, 287 (1977).
12. T. H. Dunning, Jr. and P. J. Hay, Appl. Phys. Lett. 28, 649 (1976).
13. D. W. Setser (private communication).
14. E. R. Ault, M. L. Bhaumik, and N. T. Olson, IEEE J. Quantum Electron., QE-10, 624 (1974).
15. J. Tellinghuisen, Chem. Phys. Lett. 29, 359 (1974).
16. M. V. McCusker (private communication).
17. R. S. Bradford, Jr., W. B. Lacina, E. R. Ault, and M. L. Bhaumik, Optics Commun. 18, 210 (1976).
18. O. Judd, J. Appl. Phys. 47, 5297 (1976).

19. W. B. Lacina, presented at Second Winter Colloquium on Laser-Induced Chemistry, Park City, Utah, 1977.
20. W. H. Long, Jr., W. F. Bailey, and A. Garscadden, *Phys. Rev. A*, 13, 471 (1976).
21. I. P. Shkarofsky, T. W. Johnson, and M. P. Bachynski, *The Particle Kinetics of Plasmas*, (Addison-Wesley Publishing Company, 1966), p. 283.
22. H. B. Milloy, R. W. Crompton, J. A. Rees, and A. G. Robinson, in *Abstracts of Papers of the 9th ICPEAC*, ed. J. S. Risley and R. Geballe, (University of Washington Press, Seattle, 1975) Vol. 1, p. 457.
23. L. S. Frost and A. V. Phelps, *Phys. Rev.* 136, A1538 (1964).
24. M. Schaper and H. Scheibner, *Beit. Plasma Phys.* 9, 45 (1969).
25. J. H. Jacob and J. A. Mangano, *Appl. Phys. Lett.* 29, 467 (1976).
26. D. Rapp and P. Englander-Golden, *J. Chem. Phys.* 43, 1464 (1965).
27. T. N. Rescigno and C. F. Bender, *J. Phys. B*, 9, L329 (1976).
28. P. Mahadevan, M. Epstein, and R. Hofland, presented at Second Winter Colloquium on Laser-Induced Chemistry, Park City, Utah, 1977.
29. J. L. Pack, R. E. Voshall, and A. V. Phelps, *Phys. Rev.* 127, 2084 (1962).
30. A. G. Robertson, in *The Diffusion and Drift of Electrons in Gases*, L. G. H. Huxley and R. W. Crompton (John Wiley & Sons, New York, 1974), p. 607.
31. J. Brambring, *Z. Phys. (Germany)*, 179, 539 (1964).
32. J. D. Daugherty, J. A. Mangano, and J. H. Jacob, *Appl. Phys. Lett.* 28, 581 (1976).
33. R. Burnham and S. K. Searles, *J. Chem. Phys.* 67, 5967 (1977).
34. H. H. Nakano, R. M. Hill, D. C. Lorents, D. L. Huestis, and M. V. McCusker, SRI Report No. MP 76-99 (1976).